HHS Public Access

Author manuscript

Cancer Cell. Author manuscript; available in PMC 2019 September 10.

Published in final edited form as:

Cancer Cell. 2018 September 10; 34(3): 453–465.e9. doi:10.1016/j.ccell.2018.08.006.

MEF2B instructs germinal center development and acts as an oncogene in B cell lymphomagenesis

Paola Brescia[1], **Christof Schneider**[1,^], **Antony B. Holmes**[1], **Qiong Shen**[1], **Shafinaz Hussein**[2], **Laura Pasqualucci**[1,3,6], **Katia Basso**[1,3,7,*], and **Riccardo Dalla-Favera**[1,3,4,5,6,7,8,*]

[1]Institute for Cancer Genetics, Columbia University, New York, NY, 10032, USA

[2]Department of Pathology, Icahn School of Medicine at Mount Sinai, New York, NY

[3]Departments of Pathology and Cell Biology, Columbia University, New York, NY, 10032, USA

[4]Microbiology and Immunology, Columbia University, New York, NY, 10032, USA

[5]Genetics and Development, Columbia University, New York, NY, 10032, USA

[6]The Herbert Irving Comprehensive Cancer Center, Columbia University, New York, NY, 10032, USA

Summary

SUMMARY—The gene encoding the MEF2B transcription factor is mutated in germinal-center (GC)-derived B-cell lymphomas, but its role in GC development and lymphomagenesis is unknown. We demonstrate that *Mef2b* deletion reduces GC formation in mice and identify MEF2B transcriptional targets in GC, with roles in cell proliferation, apoptosis, GC confinement and differentiation. The most common lymphoma-associated MEF2B mutant (MEF2B^{D83V}) is hypomorphic, yet escapes binding and negative regulation by components of the HUCA complex and class IIa HDACs. *Mef2b*^{D83V} expression in mice leads to GC enlargement and lymphoma development, a phenotype that becomes fully penetrant in combination with BCL2 de-regulation, an event associated with human *MEF2B* mutations. These results identify MEF2B as a critical GC regulator and a driver oncogene in lymphomagenesis.

[*]Correspondence: kb451@cumc.columbia.edu , rd10@cumc.columbia.edu.
[^]Present address: Department of Internal Medicine III, Ulm University, Ulm, Germany.
[7]Senior authors.
[8]Lead contact.

AUTHOR CONTRIBUTIONS

Conceptualization, K.B. and R.D.-F.; Methodology, P.B., C.S. and K.B.; Software: A.B.H. and K.B.; Validation, P.B., K.B. and R.D-F.; Formal Analysis, P.B., A.B.H. L.P., and K.B.; Investigation, P.B., C.S., Q.S., S.H., K.B.; Writing - Original Draft, P.B., K.B. and R.D-F.; Writing – Review and Editing, P.B., C.S., A.B.H., S.H., L.P., K.B. and R.D-F.; Visualization, P.B., A.B.H., S.H. and K.B.; Supervision, K.B. and R.D-F.; Project Administration, K.B. and R.D-F.; Funding acquisition, L.P., K.B. and R.D-F.

DECLARATION OF INTERESTS

The authors declare no competing interests.

DATA AND SOFTWARE AVAILABILITY

Accession Numbers

RNA-seq and ChIP-seq data are available in the GEO database as series GSE110669, GSE110676, GSE110682.

SIGNIFICANCE—*MEF2B* is mutated in ~15% of Follicular Lymphoma and Diffuse Large B cell Lymphoma, the most common types of mature B cell malignancies. Here we establish a critical physiologic role of MEF2B in the development of GC B cells, the cell-of-origin of most human B cell lymphomas. Modeling the expression of the most frequent lymphoma-associated *MEF2B* mutant allele in mice, we demonstrate that mutant MEF2B contributes to lymphomagenesis *in vivo* and identify the involved biochemical mechanism. MEF2B mutant-driven mouse lymphomas represent a faithful model of the human disease for pre-clinical therapeutic testing.

IN BRIEF

Brescia et al. show that MEF2B is critical for germinal center (GC) formation and identify MEF2B transcriptional targets in GC B cells. They also characterize the most common lymphoma-associated MEF2B mutant (MEF2B^{D83V}) and demonstrate that MEF2B^{D83V} leads to GC enlargement and lymphoma development in mice.

Graphical Abstract

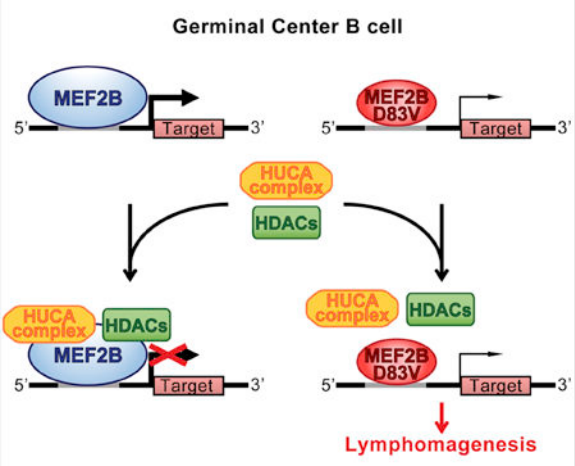

INTRODUCTION

Diffuse Large B Cell Lymphoma (DLBCL) and Follicular Lymphoma (FL) are the two most common forms of mature B cell lymphoid neoplasms, accounting for over 50% of all diagnoses (1997; Swerdlow, 2016). Both tumors derive from B cells at the germinal center (GC) stage of differentiation. Upon engagement by an antigen B cells proliferate rapidly and form GC structures. In the GC, B cells hypermutate their immunoglobulin genes in the dark zone (DZ) and are then selected based on the expression of high affinity immunoglobulin receptors in the light zone (LZ), prior to differentiation into memory B cells or plasma cells (Basso and Dalla-Favera, 2015).

An expanding body of genomic studies has identified numerous somatic genetic alterations that are recurrently associated with mature B cell lymphoma pathogenesis often by contributing to the dysregulation of pathways involved in GC physiology (Basso and Dalla-Favera, 2015; Shaffer et al., 2012). Among these alterations, are prominent those affecting transcription factors that are deputed to the control of the GC initiation, DZ to LZ re-

circulation, and GC exit. Nonetheless, a number of recurrently altered transcription factors remains unexplored in their normal and pathological function, while they are candidate drivers in mature B cell lymphoma pathogenesis and potential therapeutic targets.

The gene encoding the MEF2B transcription factor is somatically mutated in approximately 15% of DLBCL and FL (Lohr et al., 2012; Morin et al., 2011; Okosun et al., 2014; Pasqualucci et al., 2014; Pasqualucci et al., 2011; Reddy et al., 2017; Zhang et al., 2013) and in a small fraction (~3%) of Mantle Cell Lymphomas (Bea et al., 2013). Nonetheless, the role of MEF2B in normal B cell, and specifically in GC development, as well as its oncogenic potential remain largely unexplored. MEF2B belongs to the MEF2 (Myocyte Enhancer Factor 2) family of transcription factors, which includes three additional members, MEF2A, MEF2C and MEF2D, initially identified as important regulators of myocyte differentiation (Gossett et al., 1989; Potthoff and Olson, 2007). MEF2 proteins are characterized by a highly similar N-terminus including a MADS and a MEF domain that are required for DNA binding, dimerization and interaction with co-factors (Han et al., 2005; Han et al., 2003; Lu et al., 2000b; Youn and Liu, 2000). Conversely, the C-terminal transactivation domain is divergent among the MEF2 family members and subject to a complex pattern of alternative splicing (Potthoff and Olson, 2007). MEF2B itself is expressed in at least two isoforms (A and B) with distinct C-terminal domains. MEF2 proteins are highly expressed in muscle and brain, but are also detected in lymphocytes, and their expression in many cell types occurs concomitantly with the activation of differentiation programs (Potthoff and Olson, 2007).

We previously showed that MEF2B is highly expressed in GC B cells, where it directly transactivates BCL6 (Ying et al., 2013), a transcriptional repressor that is required for GC formation and the de-regulation of which leads to lymphomagenesis (Basso and Dalla-Favera, 2010). We established that the majority of mutations affecting the MEF2B N-terminus abrogates the ability of MEF2B to interact with the co-repressor CABIN1 and therefore to respond to its negative modulation of transcription. Conversely, mutations targeting the C-terminus of MEF2B have been associated with escape from phosphorylation-mediated negative regulation (Ying et al., 2013). Although these observations are consistent with an activating phenotype associated with *MEF2B* mutations, a loss of function role has been proposed, based also on the report of rare chromosomal deletions encompassing the *MEF2B* locus (Pon and Marra, 2016; Pon et al., 2015). Overall, the role of MEF2B in normal GC B cell development and its contribution to lymphomagenesis remains unknown.

Here we investigate the role of MEF2B in GC physiology and the contribution to lymphomagenesis of the most frequent lymphoma-associated *MEF2B* mutation *in vivo*.

RESULTS

GC-specific deletion of *Mef2b* reduces GC formation

In order to investigate the role of MEF2B during GC development, we generated a conditional knock-out mouse model in which all coding exons of *Mef2b* were specifically deleted in GC B cells by crossing with transgenic mice expressing the Cre recombinase under the control of the Cγ1 promoter (Casola et al., 2006).

Mef2b wild-type (*Mef2b*$^{+/+}$;*Cγ1*$^{cre/+}$), heterozygous (*Mef2b*$^{fl/+}$;*Cγ1*$^{cre/+}$) and knock-out (*Mef2b*$^{fl/fl}$;*Cγ1*$^{cre/+}$) littermates were analyzed 10 days after immunization with sheep red blood cells (SRBC). Efficient deletion of *Mef2b* was confirmed in GC B cells from *Mef2b*$^{fl/fl}$;*Cγ1*$^{cre/+}$ mice by immunofluorescence analysis on spleen sections displaying, as expected, only occasional cells escaping cre-mediated deletion (<2% of the GCs) (Figure S1A). Although GC development was observed in all mice, *Mef2b*-null GC B cells were significantly reduced compared to wild-type littermates (Figures 1A and S1B), while no significant differences were observed in other mature B cell subpopulations including follicular and marginal zone B cells (Figure S1C). The reduced percentage of GC B cells observed by cytofluorimetric analysis (Figures 1A and S1B) was consistent with the presence of fewer and smaller MEF2B-null GCs, detected by immunohistochemical and immunofluorescence analysis of PNA-stained spleen sections (Figures 1B and 1C). The absolute number of GC B cells was also reduced, but did not reach statistical significance, most likely due to the limited number of animals (Figure S1D). In addition, GC B cells from *Mef2b*-deficient mice displayed slightly reduced levels of BCL6, which were detectable by cytofluorimetric analysis (Figure 1D), but not by less sensitive assays such as immunohistochemistry (Figure 1C) or immunoblotting (data not shown). Since MEF2B directly transactivates BCL6 (Ying et al., 2013), this finding suggests functional redundancy by other MEF2 factors (see below).

The assessment of DZ (CXCR4^{high}, CD86^{low}) and LZ (CD86^{high}, CXCR4^{low}) GC B cells showed a reduced DZ/LZ ratio in *Mef2b*-deficient mice (Figures 1E and S1E). Gene Set Enrichment Analysis (GSEA) performed on expression data from *Mef2b* wild-type and *Mef2b*-null GC B cells using previously reported DZ/LZ gene signatures (Victora et al., 2012), showed that *Mef2b*-null GCs were enriched for genes induced in LZ B cells, while DZ-induced genes were negatively affected (Figure 1F). Cell quantification in the DZ and LZ compartments showed a significantly decreased number of DZ B cells in absence of *Mef2b*, while LZ cells remained unchanged, suggesting that *Mef2b* deletion affects mainly the DZ compartment (Figure 1G). Nonetheless, both somatic hypermutation and class switch recombination were normal in *Mef2b*-null GC B cells (Figures S1F, S1G and S1H). Together these results indicate that MEF2B promotes normal GC development, in particular of the DZ compartment.

The defect in GC formation observed in *Mef2b*-deficient mice is only partial (Figure 1), likely due to functional redundancy between MEF2B and other MEF2 family members, all of which are expressed in GC B cells, although only MEF2B is expressed exclusively at the GC stage (Figure S2A). In order to test the overall role of the MEF2 family in GC formation, we generated mice with GC-specific deletion of each MEF2 family member (*Mef2a*, *Mef2b*, *Mef2c* and *Mef2d*) alone or in combination. Consistent with previous reports (Khiem et al., 2008; Wilker et al., 2008), *Mef2c*-deficient mice displayed impairment of GC formation (Figure S2B) and, similarly to *Mef2b*-deficient animals, lower levels of BCL6 protein (Figure S2C). Co-deletion of *Mef2b* and *Mef2c* dramatically reduced the percentage of GC B cells (Figure S2D). Individual deletion of the remaining two members, *Mef2a* and *Mef2d*, did not impair significantly GC formation, while deletion of both genes had a modest, but significant effect (Figure S2E). However, only deletion of all MEF2 family members completely abrogated GC formation (Figure S2F), the few GCs detected in

MEF2-deficient mice being the result of incomplete cre-mediated deletion (Figure S2G). Overall, these results indicate that MEF2 expression is required for GC formation.

MEF2B predominantly binds to GC-specific enhancer regions

Toward the identification of the MEF2B-driven transcriptional network, we first determined the chromatin binding profile of MEF2B by ChIP-seq analysis in human GC B cells isolated from tonsil tissue of two independent pools of donors. This analysis identified about 20,000 MEF2B binding peaks, of which 15% were associated with promoter regions (−2/+1 kb from the TSS), 35% were intragenic and 50% were in intergenic regions (Figure 2A and Table S2). The large majority of the bound regions displayed histone marks suggestive of active promoters (H3K4me3^{+} and H3K27Ac^{+}) or enhancers (H3K4me1^{+} and H3K27Ac^{+} intergenic or intragenic peaks) (Figure 2A and 2B) (Creyghton et al., 2010; Ernst et al., 2011; Heintzman et al., 2007; Mikkelsen et al., 2007). In fact, about 60% of MEF2B-bound regions overlapped with enhancers and super-enhancers, as identified by the ROSE algorithm applied to H3K27Ac data generated on the same GC B cell pools (Loven et al., 2013; Whyte et al., 2013) (Figure 2C). Indeed, MEF2B was bound to 68% of the 9,294 predicted enhancers and to all the 655 super-enhancers that we identified in GC B cells (Zhang et al., 2017) (Figure 2D and Table S2), including those associated with the expression of several GC master regulators (BCL6, IRF8, FOXO1) and modulators of B cell fate (PAX5, BACH2) (Basso and Dalla-Favera, 2015). MEF2B-bound regions were significantly enriched in MEF2 DNA binding motifs, as well as in motifs of several transcription factors that are involved in the GC reaction including IRF, STAT and ETS family members, suggesting a coordinated role in GC development and function (Table S3). In conclusion, MEF2B binds extensively to GC B cell regulatory elements at both promoters and distal predicted enhancers, including the totality of GC super-enhancers.

MEF2B modulates genes involved in cell cycle, DNA replication and repair, apoptosis and GC B cell confinement

In order to pinpoint direct MEF2B targets, we aimed at identifying genes that display evidence of both binding in their regulatory regions and transcriptional changes in response to MEF2B expression levels. Toward this end, we integrated ChIP-seq data generated from human GC B cells with RNA-seq data from human B cell subpopulations (naive, GC and memory B cells) and *Mef2b* knock-out mice (Figure 3A). The results showed that ~60% of the MEF2B-bound genes were significantly up- (2,464 genes) or down-regulated (2,009 genes) in human GC B cells (MEF2B^{+}) compared to naïve and memory B cells (MEF2B^{-}) (Table S4). Genes bound and transcriptionally modulated in human GC B cells were further intersected with the genes differentially expressed between mouse MEF2B-null and wild-type GC B cells. This analysis yielded a “core” of targets that displayed evidence of MEF2B binding in their regulatory regions and were up- (141 genes) or down-regulated (109 genes) in the presence of MEF2B both in human and mouse GC B cells (Figure 3A and Table S4).

Pathway enrichment analyses combined with manually curated annotations of the “core” target genes supported a role for MEF2B in multiple pathways relevant to GC biology including DNA replication and repair, cell cycle, apoptosis and GC B cell confinement (Figure 3B). In addition, MEF2B modulated the expression of several transcription factors

with a role in B cell differentiation, including PAX5 and BCL6 (Ying et al., 2013). Moreover, MEF2B targets included epigenetic modifiers potentially involved in the establishment of a coherent chromatin re-modeling program. In this context, PRC2-associated factors (MTF2 and PHF19), which are involved in the deposition of silencing chromatin methylation marks, are up-regulated by MEF2B, while KDM7A, a H3K27 and H3K9 demethylase is down-regulated in GC B cells. Overall, these results support a direct role of MEF2B in promoting functions that are critical for the development of the GC and, in particular, the DZ.

The most common lymphoma-associated MEF2B^{D83V} mutant is hypomorphic

The most common *MEF2B* mutation associated with FL and DLBCL leads to the D83V amino acid change in the MEF2 N-terminus (Ying et al., 2013). In order to examine the function of this mutant, we engineered a DLBCL cell line (SUDHL10) to express a double-tagged (HA and FLAG) wild-type (SUDHL10-MEF2B^{WT}) or mutant (SUDHL10-MEF2B^{D83V}) MEF2B. ChIP-seq analyses of these cell lines using antibodies against the tags (anti-HA and anti-FLAG) or against MEF2B protein identified loci bound either by exogenous (MEF2B^{WT} or MEF2B^{D83V}) or by both endogenous and exogenous, MEF2B proteins. This analysis showed that the overall number and identity of MEF2B-bound regions was virtually identical in the two isogenic cell lines, regardless of the mutant presence (Figure 4A and Table S5). However, MEF2B^{D83V} displayed a reduced ability to bind and/or reside on DNA, as shown by the fewer bound regions (2,692 vs 7,127) that were detected in the ChIP-seq data generated by immunoprecipitation of the exogenous FLAG-HA-tagged proteins (Figure 4B and Table S5). Yet, no significant differences were detected in the peak distribution among promoters, intragenic and intergenic regions (Figure S3A-B) or in the binding motifs when comparing the regions occupied by MEF2B^{WT} or MEF2B^{D83V}, indicating that the mutant protein recognizes the same DNA sequences as the wild-type (Figure 4B). Consistent with previous data (Pon et al., 2015), electrophoresis mobility gel shift assay also identified a reduced DNA binding of MEF2B^{D83V} protein (data not shown).

Previous observations in non-B cell systems suggested that MEF2B^{D83V} is less stable compared to MEF2B^{WT} (Pon et al., 2015). We thus explored whether this feature was maintained in B cells by measuring the MEF2B^{WT} and MEF2B^{D83V} protein half-life in two DLBCL cell lines (Figure S3C). Although MEF2B isoform B appeared to have a longer half-life compared to isoform A, both MEF2B^{D83V} isoforms displayed a 30% reduction in protein stability (Figures 4C and S3D). Notably, multiple mutants targeting the MEF2/MADS domain display similarly reduced half-life (Figure S3E), suggesting that these features are shared by most N-terminus DLBCL-associated MEF2B mutants. Together, these results demonstrate that the MEF2B^{D83V} mutant displays hypomorphic features that may contribute to its partially impaired transcriptional activity (see below).

The MEF2B^{D83V} mutant escapes binding and negative regulation by co-repressor complexes

We previously reported that MEF2B^{D83V}, as well as most of the MEF2B N-terminus mutants detected in human DLBCL, cannot interact with the co-repressor CABIN1 (Ying et

al., 2013). In order to comprehensively identify interactors that may regulate MEF2B activity and may be affected by the D83V amino acid change, we performed mass-spec analysis on the proteins co-immunoprecipitated from the SUDHL10-MEF2B^{WT} and -MEF2B^{D83V} cells. This analysis showed that the MEF2B^{WT} and MEF2B^{D83V} protein complexes are quite similar, except for a very small subset of key interactors that could be assigned to two groups: the HUCA complex (Tagami et al., 2004), including CABIN1, HIRA, UBN1 and ASF1a; and the HDAC class IIa members, namely HDAC4, HDAC5, HDAC7 and HDAC9 (Figure S4A).

Interactions with MEF2B^{WT}, but not with MEF2B^{D83V}, were confirmed by co-immunoprecipitation for all the HUCA complex members and for HDAC5 and HDAC7 (Figures 5A, S4B, S4C and S4D). Although confirmed as MEF2B interactors in transiently transfected 293T cells (Figure S4E), the remaining members of HDAC class IIa identified by mass-spec analysis (HDAC4 and HDAC9) were not validated in B cells, possibly due to their lower expression levels (Figure S4F). Importantly, analysis of normal human GC B cells, showed that MEF2B forms stable interactions with the HUCA complex members, as well as with HDAC5 and HDAC7, thus confirming their physiologic relevance (Figure 5B). In addition, co-immunoprecipitation of endogenous MEF2B with its interactors was present, but reduced, in cell lines carrying a heterozygous *MEF2B*^{D83V} allele, consistent with the presence of a *MEF2B*^{WT} allele (Figure 5C).

In order to test the effect of these interactors on MEF2B transcriptional activity, we performed luciferase reporter assays. As expected, co-transfection of the reporter with plasmids expressing MEF2B^{WT} or MEF2B^{D83V} led to increased luciferase activity, which was effectively abrogated when using a MEF2B mutant lacking the MADS/MEF2 domains (MEF2B$^{\Delta\Delta}$), or a mutated version of the reporter with disrupted MEF2B binding sites (Figure 5D). Consistent with its hypomorphic features, MEF2B^{D83V} transcriptional activity was reduced compared to that of MEF2B^{WT}. The MEF2B^{WT}-driven induction was efficiently abrogated in the presence of HDAC5, HDAC7 or CABIN1, but not by a CABIN1 mutant (L2172A) that does not bind to MEF2B. In contrast, MEF2B^{D83V} transcriptional activity was insensitive to each of these negative modulators (Figure 5D).

Overall, the impaired interaction of the MEF2B^{D83V} mutant with multiple negative regulators of MEF2B transcriptional activity suggests that this mutant, although hypomorphic, may act dominantly by escaping negative modulation.

The MEF2B^{D83V} mutant enhances GC formation in mice

In order to investigate the impact of MEF2B^{D83V} in normal GC development, we generated a conditional *Mef2b*^{D83V} knock-in mouse model by introducing in the endogenous *Mef2b* locus a loxP-STOP-loxP cassette followed by the exon 3 harboring the mutation that leads to the D83V amino acid change (Figure S5A). These mice were crossed with the Cγ1-cre line (Casola et al., 2006) to induce the removal of the STOP cassette and the consequent expression of the mutant allele in GC B cells. The mutation abrogates an EcoRV restriction site and therefore expression of the mutant allele can be detected by RT-PCR followed by EcoRV digestion of the PCR product (Figure S5B and S5C).

Since lymphoma-associated *MEF2B* mutations are always found in heterozygosity, we analyzed mice expressing in GC B cells the *Mef2b*^{D83V} allele in combination with a wild-type allele (*Mef2b*$^{+/stopD83V}$;Cγ1$^{cre/+}$, WT/D83V). In addition, in order to address the genetic mechanisms underlying the activity of the *Mef2b*^{D83V} allele, we examined littermates expressing mono-allelic wild-type (*Mef2b*$^{fl/+}$;*Cγ1*$^{cre/+}$, -/WT) or mutant *Mef2b* (*Mef2b*$^{fl/stopD83V}$;*Cγ1*$^{cre/+}$, -/D83V). Ten days upon SRBC immunization no differences were observed in the non-GC B cell compartments (Figure S5D), while a significant increase in GC B cells was detected for both the WT/D83V and -/D83V mice compared to wild-type (*Mef2b*$^{+/+}$;*Cγ1*$^{cre/+}$, WT/WT) controls (Figures 6A and S5E). In the presence of MEF2B^{D83V}, GCs were significantly larger, as detected by immunohistochemical and immunofluorescence analysis of PNA on spleen sections (Figures 6B and 6C). The absolute number of GC B cell displayed a clear trend toward an increase, which did not reach statistical significance most likely due to the limited number of animals (Figure S5F). The DZ/LZ ratio was significantly reduced compared to wild-type mice (Figures 6D and S5G), and GSEA using previously reported DZ/LZ gene signatures (Victora et al., 2012), showed that MEF2B^{D83V} GCs are relatively enriched for genes induced in LZ B cells, while they appear depleted for genes induced in the DZ B cells (Figure 6E and Table S6). In presence of MEF2B^{D83V}, the number of LZ, but not of DZ, B cells was increased (Figure 6F), suggesting that, in contrast with the MEF2B-null GCs, which showed reduction of the DZ compartment (Figure 1G), the decreased DZ/LZ ratio in mice expressing MEF2B^{D83V} is due to an expansion of the LZ. Notably, hemizygosity of the WT allele (-/WT) does not affect or modestly reduces GC, and in particular DZ, formation (Figures 1 and 6), while hemizygosity of the mutant allele (-/D83V) leads to increased GC formation (Figures 6A, 6B and 6C) and LZ expansion (Figure 6F). Thus, the - /D83V mice fully mimicked the phenotype of WT/ D83V mice including the increased number of GC B cells and reduced DZ/LZ ratio due to LZ expansion, consistent with a dominant behavior.

In order to test whether the hypomorphic features observed in B cell lines (Figure 4) were trackable *in vivo*, we investigated the effect of MEF2B^{D83V} on the expression of the MEF2B "core" targets in mouse GC B cells. GSEA showed that the MEF2B "core" targets were concordantly but inefficiently modulated by the MEF2B^{D83V} mutant compared to MEF2B^{WT}, suggesting a reduced ability of MEF2B^{D83V} to transcriptionally regulate MEF2B targets *in vivo*, consistent with its hypomorphic nature (Figure 6G and Table S6). In conclusion, the *Mef2b*^{D83V} mutant behaves as a hypomorphic dominant allele *in vivo* to increase GC formation by expanding the LZ B cell compartment.

In order to investigate the overall transcriptome changes induced by the expression of the *Mef2b*^{D83V} mutant *in vivo*, we identified the genes differentially expressed in GC B cells of WT and mutant (+/D83V and -/D83V) mice. The MEF2B^{D83V}-driven signature included DZ- and LZ-associated genes (Victora et al., 2012; Victora et al., 2010), which were enriched in WT and MEF2B^{D83V} GC B cells, respectively (consistent with Figure 6E), as well as genes not previously identified as DZ/LZ discriminators (Table S7). Pathway enrichment analysis showed that transcriptional changes induced by MEF2B^{D83V} lead to enforcement of a LZ phenotype by promoting pathways downstream of BCR and NF-κB, cell anabolism and RNA biogenesis, while inhibiting DZ features as proliferation and cell

cycle (Figure 6H and Table S8). These data confirm that expression of MEF2B^{D83V} in GC B cells enforces the establishment of a pathologically enhanced LZ transcriptional program.

The MEF2B^{D83V} mutant causes B cell lymphomas in mice

In order to address the role of MEF2B^{D83V} in lymphomagenesis, the conditional *Mef2b*^{D83V} knock-in mouse model, was crossed with *Cd21*^{cre} transgenic mice (Kraus et al., 2004), which were chosen to ensure that the locus was already suitable for expression as soon as *Mef2b* transcription is activated at the initial stages of GC commitment and slightly earlier than Cγ1 promoter activation.

As observed in *Mef2b*$^{+/stopD83V}$;*Cγ1*$^{cre/+}$ (WT/D83V) mice (Figure 6A), young *Mef2b*$^{+/stopD83V}$;*Cd21*$^{cre/+}$ mice displayed a significant increase in GC B cells compared to control littermates upon a single SRBC immunization (Figures 7A and S6A), while no differences were observed in any other B cell subpopulations. In order to investigate tumor development, mice were chronically immunized (every 2 months, for six times in total). Although no animals showed signs of disease before the end-point of the study at 17–18 months of age, at necropsy 28% (6/21) of mice displayed enlarged lymph nodes, in particular mesenteric lymph nodes, and occasionally splenomegaly. Histo-pathological analyses revealed that mice expressing MEF2B^{D83V} were affected by lymphomas originating from GC-experienced B cells and resembling human DLBCL or FL (Figures 7B and S6B). These tumors displayed expression of both mutated and WT MEF2B, mimicking the expression pattern observed in human lymphomas (Figure S6C). The tumors were clonal and GC-experienced, as shown by the presence of clonally rearranged (Figure S6D) and hypermutated Ig loci. A few tumors were also detected in mice carrying the silent *Mef2b*^{D83V} allele and lacking expression of Cre (*Mef2b*$^{+/stopD83V}$;*Cd21*$^{+/+}$) (Figure S6B). Since these tumors displayed unexpected leakage of *Mef2b*^{D83V} expression, as shown by RT-PCR followed by EcoRV digestion (Figure S6C) no further characterization was performed.

Since *MEF2B* mutations significantly co-segregate with *BCL2* re-arrangements in human DLBCL and FL cases (Morin et al., 2011; Pasqualucci et al., 2014; Pasqualucci et al., 2011), we investigated the potential cooperation between aberrant BCL2 expression and mutant MEF2B^{D83V} by crossing the conditional *Mef2b*^{D83V} knock-in mice (*Mef2b*$^{+/stopD83V}$;*Cd21*$^{cre/+}$) with *Bcl2-Ig* transgenic mice which carry a minigene mimicking the translocated *BCL2* allele found at the t(14;18) breakpoint in human FL (McDonnell et al., 1989). These mice displayed an increased probability of developing GC-experienced lymphomas (Figures 7B and 7C), which maintained the expression of both the WT and the mutant *Mef2b* allele (Figure S6E). As expected, ~40% (6/16) of *Bcl2-Ig* mice developed FL by 17–18 months of age (Figure 7B). In addition, ~20% (3/16) of *Bcl2-Ig* mice displayed clonal neoplasms with large cells characterized by a lack of B cell markers (B220^{-}/PAX5^{-}/BCL6^{-}) and expression of plasmacytic differentiation markers including IRF4 (Figure 7D) and CD138 (data not shown), suggesting that they may represent a counterpart of human plasmablastic lymphoma (PBL). Notably, co-expression of de-regulated BCL2 and MEF2B^{D83V} markedly increased the incidence of lymphomas leading to an almost fully penetrant tumor phenotype, with over 90% of *Mef2b*^{D83V};*Bcl2* compound mice developing

GC-experienced lymphomas (Figure 7B) that were clonal (Figure S6F) and resembled the human diseases morphologically, phenotypically (Figure 7D) and in late age appearance (Figure 7C). The presence of somatic hypermutation in the clonally rearranged IgV loci further confirmed the origin from GC-experienced cells of all FL and DLBCL tumors tested. PBL included both IgV-mutated and -unmutated cases, suggesting that these malignancies may originate from both GC-experienced and -unexperienced B cells. However, PBL develop exclusively in association with de-regulated BCL2 expression, regardless of the presence of the *Mef2b*^{D83V} allele, indicating that they are not pathogenetically related to MEF2B. Taken together these results indicate that the *Mef2b*^{D83V} allele causes lymphomas originating from GC-experienced B cells.

Tumors from the *Mef2b*^{D83V};*Bcl2* compound mice displayed more aggressive features compared to tumors from the *Mef2b*^{D83V} mice, as shown by: (i) early onset, with several mice being euthanized as early as 14 months of age; (ii) disseminated disease, involving multiple lymph nodes, spleen, intestine and bone marrow; (iii) presence of multiple tumors, that arose in the same or in different organs, and were occasionally proven to originate from distinct malignant clones (Figure 7C and S6F). Overall, these results show that MEF2B^{D83V} mutant contributes to lymphomagenesis *in vivo* and synergizes with BCL2 ectopic expression, leading to a fully penetrant tumor phenotype resembling the human FL/DLBCL spectrum associated with MEF2B mutations.

DISCUSSION

The first conclusion derived from our results is that MEF2B has a role in GC development, in particular in the formation of the DZ, the site where antigen-activated B cells clonally expand and undergo somatic hypermutation of their immunoglobulin genes. This observation is consistent with MEF2B pattern of expression, starting in the initial cell divisions at the onset of the GC reaction and peaking in GC B cells (Ying et al., 2013). GC-specific deletion of MEF2B, however does not lead to complete abrogation of GC, a finding analogous to MEF2C inactivation (Khiem et al., 2008; Wilker et al., 2008). Since MEF2C is expressed at all mature B cell stages, and can form hetero-dimers with other MEF2 family members (Black and Olson, 1998), including MEF2B, it is conceivable that these two molecules may be at least in part functionally redundant. This notion is supported by our observation that deletion of all MEF2 family members (*Mef2a*, *Mef2b*, *Mef2c* and *Mef2d*) in GC B cells completely abrogates GC formation (Figure S2). Further investigations are needed to fully dissect the crosstalk of MEF2 family members during the GC reaction.

The binding profile of MEF2B in the genome of GC B cells, characterized by extensive enhancer occupancy including the full set of GC-specific super-enhancers, suggests that MEF2B works as a main mediator of the GC-specific transcriptional program. We previously showed that MEF2B modulates the expression of the GC master regulator BCL6 by direct binding to its promoter (Ying et al., 2013). This finding is confirmed by the present study and by the observation that MEF2B binds also to two super-enhancer regions that have been shown to be part of an anchoring center responsible of BCL6 expression (Bunting et al., 2016; Ryan et al., 2015). However, in apparent discrepancy with these findings, we report here that MEF2B-null GC B cells display only mild reduction of BCL6 expression.

We interpret this result as due to the compensatory action of other MEF2 family members, consistent with their overall redundant role in GC formation. Thus, a conclusive elucidation of whether BCL6 is required for the physiologic role of MEF2B awaits the results of experiments reconstituting BCL6 expression in B cells of mice lacking all MEF2 genes. Nonetheless, MEF2B may have a role in GC physiology extending beyond the induction of BCL6 expression since the MEF2B transcriptional program includes many genes that are critical to GC development but are not controlled by BCL6. Furthermore, MEF2B is bound on all GC-specific super-enhancers, including those associated with multiple GC master regulators (BCL6, IRF8, FOXO1) and modulators of B cell fate (PAX5, BACH2) (Basso and Dalla-Favera, 2015).

Our analysis has explored the functional features of the most common mutation associated with FL and DLBCL and has shown that the MEF2B^{D83V} mutant protein carries two main traits distinguishing it from its wild-type counterpart. First, the mutant protein is hypomorphic, as documented by its decreased binding to DNA and half-life, as well as reduced transcriptional activity. These results, obtained in B cells, confirm and extend previous observations in non-B cell systems (Pon et al., 2015). Second, we show that MEF2B^{D83V} mutant fails to bind and thus escapes repression by the HUCA complex, extending previous observations relative to the HUCA component CABIN1 (Ying et al., 2013), and by several class IIa HDACs. Notably, the interaction of MEF2D, and likely of other MEF2 family members, with CABIN1 and class IIa HDACs is modulated by calcium signaling, which leads to calmodulin-dependent release of CABIN1 and class IIa HDACs and promotes their nuclear export leading to MEF2D activation (Lu et al., 2000a; McKinsey et al., 2000; Pan et al., 2005; Youn and Liu, 2000). If confirmed to act also in B cells on MEF2B, this mechanism would imply that MEF2B^{D83V}, as well as other mutants that cannot bind HUCA and HDACs, represent constitutively active forms of MEF2B.

The hypomorphic features of the MEF2B^{D83V} mutant do not interfere with the normal function of MEF2B, as shown by the normal DZ development in mice expressing MEF2B^{D83V} also in the absence of MEF2B^{WT}. However, the lack of interaction with its negative regulators may prevent the modulation of MEF2B^{D83V} activity normally occurring in the LZ, leading to the expansion of this compartment and the establishment of an enforced activated phenotype. Thus, although hypomorphic, the key feature of the pathologic function of the MEF2B^{D83V} mutant appears to be its dysregulated constitutive activity, irresponsive of negative regulation, a notion supported by the observation that several other mutants, specifically those affecting the MEF2 domain, are both hypomorphic (Figure S3E) and fail to bind co-repressor molecules (Ying et al., 2013). We speculate that the hypomorphism may reflect a common conformational change affecting the N-terminus region and/or a transformation-associated selective pressure toward mutants that are dysregulated but limited in the extent of their activity. This notion is supported by recent crystallographic analyses of the MEF2B^{D83V} mutant revealing that the D83V amino acid change induces a dramatic α-helix to β-strand switch in the MEF2 domain. This conformational change is consistent with a modest impact on the DNA binding properties of the protein, but dramatically affects the domain involved in the interaction with co-factors (Lei et al., 2018).

The results herein provide evidence that the MEF2B^{D83V} mutant contributes to B cell lymphomagenesis *in vivo* by acting as a dominant oncogene. Based on its hypomorphic features and on the observation of rare instances of *MEF2B* haploinsufficiency due to chromosomal deletions or non-sense truncating mutations, it has been previously proposed that MEF2B is a tumor suppressor in B cells (Pon and Marra, 2016; Pon et al., 2015). However, the evidence that the MEF2B^{D83V} mutant in hetero- or hemizygosity is associated with GC expansion and eventually lymphomagenesis, together with the observation that reduced MEF2B expression instead decreases GC formation, provides a conclusive genetic evidence excluding the tumor suppressor model.

Despite its dominant nature, the MEF2B^{D83V} mutant has relatively weak oncogenic properties as single initiating event, as shown by the low penetrance of the malignant phenotype, which is however strongly enhanced by the expression of the BCL2 oncogene. We note that the transcriptional network driven by MEF2B retains a pro-apoptotic program, including trans-repression of BCL2, which may be counteracted by BCL2 constitutive expression. The compound MEF2B^{D83V};BCL2 mouse model is representative of the genetics of a sizable fraction of human FL and DLBCL and faithfully recapitulates their spectrum of phenotypes. This mouse model represents a useful tool for studying the genetic events involved in tumor progression and as pre-clinical model for therapeutic testing.

STAR METHODS

CONTACT FOR REAGENT AND RESOURCE SHARING

Further information and requests for resources and reagents should be directed to and will be fulfilled by the Lead Contact, Riccardo Dalla-Favera (rd10@cumc.columbia.edu).

The applicant’s laboratory and institution adhere to the NIH Grants Policy on Sharing of Unique Research Resources. Specifically, mouse lines generated in the laboratory will be provided to outside investigators under the terms of a Material Transfer Agreement (MTA) from Columbia University.

EXPERIMENTAL MODEL AND SUBJECT DETAILS

Mouse models and strains—All mouse strains were backcrossed into *C57BL/6* background. Immunological responses were evaluated in immune-competent mice at 3–4 months of age. Animals assigned to the tumor cohorts were monitored twice a week for tumor incidence and survival over a period of 18 months and were killed for analysis when visibly ill or at the end of the study. Both females and males were included in the experiments. Mice were housed in a dedicated pathogen-free environment. All experiments and procedures conformed to ethical principles and guidelines revised and approved by the Institutional Animal Care and Use Committee at Columbia University.

Cell lines—HEK293T cells (female origin; American Type Culture Collection) were grown in Dulbecco’s modified Eagle medium (DMEM) supplemented with 10% fetal calf serum, 100 μg/ml penicillin and streptomycin. The male DLBCL cell lines DB, SUDHL4, SUDHL10 (Epstein et al., 1978), and the female U2932 were grown in Iscove’s modified Dulbecco’s medium (IMDM) supplemented with 10% FCS, 100 μg/ml penicillin and

streptomycin. Cell lines were maintained at 37°C in humidified incubators in the presence of 5% CO_2. All cell lines were tested negative for mycoplasma contamination.

METHOD DETAILS

Generation of *Mef2b* conditional mouse models

The conditional *Mef2b*^{fl} allele was generated by insertion of two loxP sites into intronic regions upstream of exon 2 and downstream of exon 9 by embryonic stem (ES) cell targeting. Correct homologous recombination was confirmed by Southern blotting, and the targeted mouse ES cells were injected into blastocysts derived from *C57BL/6* mice to generate chimeras. The neomycin-resistance marker, flanked by *frt* sites, was deleted by crossing to *Flp*-transgenic mice. The conditional *Mef2b*^{stopD83V} allele was generated by introducing a single nucleotide change by site directed mutagenesis leading to the D83V amino-acid change in exon 3. The neomycin-resistance marker followed by a triple-polyA, flanked by two *loxP* sites was introduced upstream the exon 3 carrying the D83V mutation. Correct homologous recombination was confirmed by Southern blotting, and the targeted mouse ES cells were injected into blastocysts derived from *C57BL/6* mice to generate chimeras. *Mef2a*$^{fl/+}$; *Mef2c*$^{fl/+}$; *Mef2d*$^{fl/+}$ mice were kindly provided by Dr. Olson (University of Texas Southwestern) and crossed with *Mef2b*$^{fl/+}$. Mice expressing the Cre recombinase under the control of the CD21 or Cγ1 promoters and *Bcl2-Ig* transgenic mice were previously described (Casola et al., 2006; Kraus et al., 2004; McDonnell et al., 1989).

Mouse immunization and analysis

In order to induce GC responses, three-month-old mice were immunized by intraperitoneal injection of 1×10^9 sheep red blood cells (SRBCs, Cocalico Biologicals) or 100 μg of NP (4-hydroxy-3-nitrophenyl-acetyl) conjugated to keyhole limpet hemocyanin (KLH, BioSearch) in complete Freund's Adjuvant (Sigma), and analyzed on days 10–12 post-immunization. To generate larger amounts of GC B cells (i.e. for gene expression profile studies), we performed two sequential injections of SRBCs (day 0, 1×10^8 SRBC; day 5, 1×10^9 SRBC) and collected cells at day 12. This protocol yielded about three-four fold more GC B cells (~12–15% of the B cell fraction). Spleens were isolated and divided into 2 fragments, which were processed for immunohistochemistry/immunofluorescence and flow cytometry, respectively. Splenic mononuclear cells were isolated by crushing the tissue through 40 μm cell strainers in ice-cold 1X phosphate-buffered saline (PBS) + 0.5% bovine serum albumin (BSA) followed by red blood cell lysis. For GC B cell isolation by cell sorting, we first performed B cell enrichment by negative selection with magnetic beads (B cell isolation kit, Miltenyi), following manufacturer's instructions. Mononuclear cell suspensions were stained for 20 minutes on ice with antigen-specific fluorochrome-conjugated antibodies (Key Resources Table). Samples were acquired on a FACSCanto II or on a FACSCalibur (BD Biosciences) and FlowJo Software (TreeStar) was used for data analyses and plot rendering. For detection of intracellular proteins, the cells were fixed and permeabilized using the BD Cytofix/Cytoperm buffer (BD Biosciences) following the manufacturer's instructions, and subsequently stained for 60 minutes at room temperature with specific antibodies (Key Resources Table).

To calculate the absolute numbers of cells within splenic B cell subsets, spleen fragments were weighed and erythrocyte-depleted mononuclear cell suspension were counted by Trypan blue exclusion using the Countess Automated Cell Counter (Thermo Fisher Scientific). The total number of counted splenic B cells was then multiplied by the fraction of each subpopulation, as identified by the cytofluorimetric analyses.

Affinity maturation and somatic hypermutation

For the analysis of somatic hypermutation events and affinity maturation, we isolated genomic DNA from sorted murine GC B cells, 12 days after NP-KLH immunization. The Ig VH186.2-JH2 segment was amplified via high-fidelity PCR, as previously described (Schwickert et al., 2009). PCR products were subcloned and single cell colonies were selected for Sanger sequencing. Sequence analysis and alignments were done with the HighV-Quest tool (The International Immunogenetics Information System, IMGT) (Lefranc, 2011). Only clones corresponding to the VH186.2 gene (IGHV 72∗01, IMGT nomenclature) were considered in the analysis.

Immunofluorescence and immunohistochemistry

For immunofluorescence, 3-μm-thick formalin-fixed, paraffin-embedded (FFPE) sections were stained using anti-MEF2B and anti-BCL6 antibodies (Key Resources Table), as previously published (Ying et al., 2013). Upon heat-induced epitope retrieval in citrate buffer (p H 6.0) tissue sections were subjected to an o/n incubation at 4°C with primary antibodies followed by repeated washes in 1X PBS+0.1% Tween20 and incubation with Cy3-conjugated secondary antibody for BCL6 detection. MEF2B immunodetection was performed by EnVision system, requiring an incubation with a polymer-enhanced horseradish peroxidase (HRP)-conjugated secondary antibody followed by tyramide-fluorochrome amplification (Agilent-Dako). Staining with biotin-conjugated anti-PNA antibody (Vector Laboratories) was performed upon heat-induced epitope retrieval in EDTA buffer (pH 8.0) by o/n incubation at 4°C followed by repeated washes in 1X PBS+0.1% Tween20 and incubation with Cy3-conjugated streptavidin or, for immnohistochemical detection, with 3-Amino-9-ethylcarbazole (AEC) substrate (Sigma). Slides were then washed and mounted (Prolong Anti-Fade Reagent, ThermoFisher Scientific). Immmunofluorescence images were captured using a Nikon Eclipse microscope and the NIS Elements software (Nikon). All images were colored, resized and merged using Adobe Photoshop software. Analysis of GC size and number was performed using ImageJ software (Schindelin et al., 2015). The GC and spleen areas were measured in pixels. Immunohistochemistry was performed on 3-μm-thick FFPE tissue sections using specific primary antibodies for PNA (described above), CD3, BCL6, BCL2, PAX5, and IRF4 and a biotin-conjugated anti-B220 antibody (Key Resources Table). Section were incubated o/n at 4°C with primary antibodies followed by repeated washes in 1X PBS+0.1% Tween20 and incubation with alkaline phosphatase (AP)-conjugated streptavidin (for B220 detection; Vector Laboratories), AP-conjugated anti-goat secondary antibodies (for PAX5 and IRF4; Southern Biotech) or a polymer-enhanced HRP-conjugated secondary antibody (for CD3, BCL2 and BCL6; EnVision system, Agilent-Dako). Upon repeated washes in 1X PBS+0.1% Tween20, detection was performed using NBT/BCIP substrate (blue color; Roche) for the AP-conjugates or AEC substrate (red color; Sigma Aldrich) for the HRP-conjugates.

Sections were also stained with hematoxylin and eosin (Thermo Fisher Scientific), according to standard procedures.

The tumor diagnosis in mice was performed by histo-pathological analysis of tissue sections according to the following criteria: i) follicular lymphoma (FL) was diagnosed based on the presence of nodular proliferation of $B220^+/BCL6^+$ B cells with centrocytic morphology (characterized by angulated/cleaved nuclei and inconspicuous nucleoli) and admixed centroblastic cells (round-ovoid nuclei and prominent nucleoli) detectable to varying degrees; ii) diffuse large B cell lymphoma (DLBCL) was diagnosed based on diffuse proliferation of medium to large $B220^+/PAX5^+$ B cells with round-ovoid nuclei, vesicular chromatin and distinct nucleoli; iii) plasmablastic lymphoma (PBL) was diagnosed in cases showing sheets of large cells with prominent nucleoli and exhibiting expression of IRF4 and absent B (B220, PAX5), GC (BCL6) or T cell (CD3) markers.

Expression vectors

The plasmids pCMV-HA-$MEF2B^{WT}$, pCMV-FLAG-$MEF2B^{WT}$, pCMV-HA-$MEF2B^{D83V}$, pCMV- FLAG-$MEF2B^{D83V}$, pCMV-HA-$MEF2B^{\Delta\Delta}$ (construct with deletion of MADS-box–MEF2 domain, residues 8–91) isoform B, and pCMV-Myc-$CABIN1^{WT}$ or pCMV-Myc-$CABIN1^{L2172A}$ mutant (residues 2037–2220) were previously reported (Ying et al., 2013). The HIRA (GeneBank accession number NM_003325.3) and ASF1a (GeneBank accession number NM_014034.2) coding sequence were amplified by PCR from cDNA of human GC B cells and subcloned into pCMV-HA expression vector (Clontech). The pQCXIP-HA-UBN1 plasmid was a gift from Dr. Peter Adams (Banumathy et al., 2009). The HDAC9 coding sequence (GeneBank accession number NM_178425.3) was amplified by PCR from cDNA of human GC B cells and was subcloned into the pCMV-FLAG expression vector (Stratagene). Plasmids pcDNA3.1-HDAC4-FLAG (13821; Addgene), pcDNA3.1-HDAC5-FLAG (13822; Addgene) and pcDNA3.1-HDAC7-FLAG (13824; Addgene) were deposited by E. Verdin (Fischle et al., 1999) in the Addgene database. MEF2B-WT or mutants (L54P, Y69H, E77K, S78R, N81Y, D83V) isoform A (NM_001145785.1) or isoform B (NM_005919) cDNAs, tagged with both FLAG and HA at the 5'-end, were subcloned into the lentiviral vector pCCL.sin.cPPT.PGK.GFP.WPRE that expresses GFP trough a bi-directional promoter (Amendola et al., 2005). The same vector expressing a FLAG-HA tag followed by a STOP codon (Empty Vector, EV) was used as negative control.

Cell transfection and lentiviral transduction

HEK293T cells were transiently transfected using polyethylenimine (PEI) (Polysciences) as previously described (Ying et al., 2013). Briefly, DNA was diluted in 150 mM NaCl and incubated with PEI for 15 min at room temperature. DNA-PEI complexes were added to the cells drop by drop. Upon incubation at 37°C for 7–8 hr, the transfection medium was removed and replaced with fresh medium. Cells were harvested 42–48 hr after transfection. Viral supernatants were obtained by transient transfection of HEK293T cells with the lentiviral vectors along with lentivirus packaging vector (Δ8.9) and a plasmid encoding vesicular stomatitis virus envelope glycoprotein (VSVg). SUDHL10 cells were infected in two rounds with viral supernatants and were sorted with a FACSAria II to obtain a pure population of infected GFP^+ cells.

Luciferase reporter assay

The luciferase reporter constructs (3xMEF2-luc) were generated by cloning into the pGL4.26 vector (Promega) the MEF2 DNA binding consensus site (CTAAAAATAA) or its mutated sequence (CTATTAATAG) in triplicates separated by an 11-base spacer. All final constructs were verified by digestion and confirmed by Sanger sequencing analysis. HEK293T cells were transiently transfected through the use of PEI (Polysciences) with pCMV-HA-MEF2B^{WT} or - MEF2B^{D83V} isoform B vectors along with the pGL4.26–3xMEF2 reporter construct and a renilla luciferase control reporter (pGL4.54-renilla) in the presence or absence of the expression vectors pCMV-myc-CABIN1^{WT} or CABIN1^{L2172A} mutant, pcDNA3.1-HDAC5-FLAG or pcDNA3.1-HDAC7-FLAG. Cells were harvested and analyzed 48 hr after transfection. Luciferase was measured using the Dual Luciferase Reporter Assay Kit (Promega) according to the manufacturer's instructions in a Glomax Multidetection Instrument (Promega).

Immunoprecipitation and immunoblotting

Whole cell protein extracts were generated from DLBCL cell lines, GC B cells isolated from human tonsils or HEK293T cells 48 hr after transfection using the following immunoprecipitation (IP) buffer: 50 mM TrisHCl pH 7.5, 150 mM NaCl, 0.2 mM EDTA pH7.0, 0.05% NP40, 0.2% TritonX-100, 30 mM beta-glycerophosphate, 0.5 mM PMSF, 50 mM sodium fluoride, 1 mM sodium orthovanadate and protease inhibitor cocktail (Sigma). Lysates were incubated overnight at 4°C with anti-FLAG or a nti-HA affinity beads (Sigma) or anti-MEF2B antibody (Key Resources Table). In the latter case lysates were supplemented with Protein G beads (GE Healthcare) for 1 h at 4°C. Bea ds were washed 5 times in the same buffer and immunocomplexes were eluted in the presence of 0.25 mg/ml FLAG or HA peptide (Sigma) or in SDS-PAGE sample-loading buffer. Eluates were resolved by SDS-PAGE, transferred on nitrocellulose membrane and, upon blocking in 1XPBS with 0.05% Tween20 and 5% non-fat dry milk for 2 hr, incubated with primary antibodies (Key Resources Table) at 4°C over-night. After washing, the membranes were incubated with horseradish peroxidase-conjugated secondary antibodies (Key Resources Table) for 2 hr at room temperature. Detection was performed by ECL Reagent (Thermo Fisher Scientific) followed by film exposure or Chemidoc Imager analysis (BioRad). ImageJ software (Schindelin et al., 2015) was used for densitometry.

Mass spectrometry analysis

MEF2B-containing protein complexes were isolated using whole-cell protein lysates from the SUDHL10 DLBCL cell lines engineered to stably express the N-terminal double-tagged FLAG- HA-MEF2B^{WT} or -MEF2B^{D83V} isoform B or a control vector. Protein extracts in IP buffer were immunoprecipitated using anti-FLAG antibody-conjugated M2 agarose beads (Sigma). Bead- bound proteins were eluted by FLAG peptide (0.25 mg/ml, Sigma) and subjected to a further step of affinity purification by incubation with anti-HA antibody-conjugated agarose beads (Sigma) followed by HA peptide (0.25 mg/ml, Sigma) elution. The eluates from the HA beads were digested with trypsin and loaded on a nano-scale reverse-phase HPLC capillary column. Eluted peptides were subjected to electrospray ionization and then entered into a LTQ Orbitrap Velos Pro ion-trap Mass Spectrometer

(ThermoFisher Scientific). Peptides were detected, isolated, and fragmented to produce a tandem spectrum of specific fragment ions for each peptide. Peptide sequences (and hence protein identity) were determined by matching protein databases with the acquired fragmentation pattern by the software Sequest (Thermo Fisher Scientific). Candidate interactor lists were pruned of non-specific interactors detected in the negative control, and then ranked based on the number of total peptides, as an estimate of protein abundance.

Protein half-life measurement

SUDHL10 and SUDHL4 cells stably expressing N-terminal double-tagged FLAG-HA-MEF2B were treated with cycloheximide (Sigma) 100 μg/ml and collected at different time points, as indicated in Figure S3D. Cells lysates were resolved by SDS-PAGE and analyzed by immunoblotting with anti-HA and anti-vinculin antibodies (Key Resources Table) as loading control. MEF2B half-life was quantified using the exponential regression function of densitometry values measured using the ImageJ processing software (Schindelin et al., 2015).

RNA extraction, cDNA synthesis, and RT-PCR

Total RNA was extracted using the Trizol Reagent (ThermoFisher Scientific), RNeasy Kit (Qiagen) or the Nucleospin RNA XS RNA Isolation Kit (Macherey-Nagel), according to themanufacturer's instructions. cDNA synthesis was performed starting with 1–3 μg of total RNA using the SuperScript II First-Strand Synthesis System (ThermoFisher Scientific). PCR was performed using the primers listed in the Key Resources Table. PCR products were analyzed by electrophoresis on agarose gels upon staining with ethidium bromide.

RNA-seq analyses

Total RNA (100 ng) was used to generate RNA-seq libraries using the TruSeq RNA Library Preparation Kit v2 (Illumina). Sequencing was performed on Hiseq 3000 (Illumina). RNA-seq reads were mapped using hisat2 (Pertea et al., 2016) with default parameters to either hg19/GRCh37 or mm10/GRCm38 using the hisat2 prebuilt genome indexes. The genome mapped reads were further mapped to exons in their respective GENCODE transcriptome references (Harrow et al., 2006) using a custom read count program. Our tool sanitizes the transcriptome references (exon only) by removing read-through genes, anti-sense elements, miRNA, and rRNA. Reads were mapped to exons based on the information in the genomic BAM files. The mapping location and CIGAR annotation string is used to break down a read into its mapped portions, to allow for insertions and deletions at splice sites, and each portion is tested for inclusion in an exon boundary. If a portion of a read overlaps an exon by a defined threshold (at least 10 bp), the read is assigned to that exon and consequently its parent gene. Our tool supports weighted fractional read mapping where appropriate. This mapping strategy is similar to those used by htseq-count (Anders et al., 2015) and featureCounts (Liao et al., 2014), two widely used aggregate count tools, but allows us to log and track the position and contribution of each read on each exon in detail. The read count tables were subsequently normalized to produce transcript per million (TPM) tables. Downstream analyses were performed using unfiltered RNA-seq data, except for GSEA displayed in Figure 6H (Table S8) for which RNA-seq data were first filtered to remove poorly expressed genes (bottom 35% based on average expression). Differential expression

analyses were performed using Student's T-test on $\log_2$(TPM+1) transformed data. Pathway enrichment analysis was performed using the DAVID 6.7 tool and KEGG, Biocarta, Panther and Reactome databases (Huang da et al., 2009).

Gene Set Enrichment Analysis

Gene Set Enrichment Analysis (GSEA) was performed using the GSEA software tool 2–2.2.0 with gene permutation and default parameters (Subramanian et al., 2005). Briefly, the enrichment score (ES) was calculated as the maximum deviation from zero of the weighted fraction of genes present minus the fraction not present up to a given index in a gene expression matrix ordered by phenotype correlation. The statistical significance (nominal p value) of the ES of a gene set was estimated using an empirical gene-based permutation test. The normalized enrichment score (NES) was calculated by creating 1,000 permutations of the ES and scaling the observed ES by the mean score of the permutations. GSEA was applied to selected gene sets to test their enrichment in a given dataset (Figures 1F, 6E and 6G). GSEA was also used to interrogate the enrichment of gene sets provided in the Molecular Signature Database (MSigDB; Collections C2 and C7) (Subramanian et al., 2005) and in the SignatureDB (https://lymphochip.nih.gov/signaturedb/) (Figure 6H).

Mouse to Human gene symbol conversion

In order to compare mouse and human data, mouse gene symbols were converted to human gene symbols using a conversion database provided from the NCBI Homologene Project (https://www.ncbi.nlm.nih.gov/homologene) using data downloaded in August 2016.

ChIP-seq analyses

Chromatin Immunoprecipitation (ChIP) was performed as previously described (Dominguez-Sola et al., 2015). Briefly, upon crosslinking with 1% formaldehyde for 10 min and quenching by addition of glycine at a final concentration of 0.125 M, cell lysis and nuclei isolation was performed using the TruChIP High Cell Chromatin Shearing Kit with SDS (Covaris). Nuclei were sonicated in the S220 Ultrasonicator (Covaris) in order to obtain chromatin fragments of 200–500 bp. Shared chromatin was incubated over-night with 4 μg of anti-MEF2B or 2 μg/each of anti-FLAG and anti-HA antibodies (Key Resources Table). Protein A magnetic beads were then added for 4 hr incubation followed by sequential washes at increasing stringency and reverse cross-linking. Upon RNAse and proteinase K treatment, ChIP DNA was purified using the MiniElute Reaction Cleanup Kit (Qiagen) and quantified using the Quant-iT PicoGreen dsDNA Reagent (Life Technologies). ChIP-seq libraries were generated starting from 4 ng of ChIP or Input DNA as reported in (Blecher-Gonen et al., 2013). Libraries were quantified using the KAPA SYBR FAST Universal qPCR Kit (KAPA Biosystems), normalized to 10 nM, pooled and sequenced in an HiSeq 2000 instrument (Illumina) as single-end 100 bp reads, obtaining on average 25×10^6 reads/sample. Sequencing data was acquired through the default Illumina pipeline using Casava V1.8. Reads were aligned to the human genome hg19 assembly (https://genome.ucsc.edu/) using the Bowtie2 aligner v2.1.0 (Langmead et al., 2009) allowing up to two mismatches. Duplicate reads (i.e., reads of identical length mapping to exactly the same genomic locations) were removed with SAMtools v0.1.19 (Li and Durbin, 2009) using the rmdup option. Peak detection was performed using ChIPseeqer v2.0 (Giannopoulou and Elemento,

2011) enforcing a minimum fold change of 2 between ChIP and input reads, a minimum peak width of 100 bp and a minimum distance of 100 bp between peaks. For ChIP performed in human GC B cells, the threshold for statistical significance of peaks was set at 10^{-12} for MEF2B and 10^{-15} for H3K4me1, H3K4me3 and H3K27Ac. H3K4me1 peaks located within ±2 kb or H3K27Ac peaks located within ±12.5 kb were subject to stitching unless mapping around a transcription start site (TSS) (±2 kb). H3K27me3 peaks were detected using RSEG (http://smithlabresearch.org/software/rseg/) with a 100 bp bin size and only peaks wider than 5 kb were considered. Enhancers and super-enhancers were identified using the ROSE algorithm (https://bitbucket.org/young_computation/rose) (Loven et al., 2013; Whyte et al., 2013) applied to the H3K27Ac ChIP-Seq data using default parameters. ROSE identifies as enhancers all H3K27Ac peaks upon stitching them when located within ±12.5 kb from each other (unless mapping ±2 kb from a TSS). ROSE ranks enhancers by their input-subtracted signal of H3K27Ac and separate them from super-enhancers by identifying an inflection point of H3K27Ac signal *versus* enhancer rank. MEF2B-bound promoters were classified based on their chromatin marks as active ($H3K4me3^+$, $H3K27me3^-$ and $H3K27Ac^+$), weak ($H3K4me3^+$, $H3K27me3^-$ and $H3K27Ac^-$), poised ($H3K4me3^+$ and $H3K27me3^+$), or inactive ($H3K4me3^-$) (Ernst et al., 2011; Mikkelsen et al., 2007). MEF2B-bound intragenic and intergenic regions were classified based on enhancer-associated chromatin marks as active ($H3K4me1^+$, $H3K4me3^-$ and $H3K27Ac^+$) or poised ($H3K4me1^+$, $H3K4me3^-$ and $H3K27Ac^-$) (Creyghton et al., 2010; Heintzman et al., 2007), while considered inactive when lacking all marks ($H3K4me1^-$, $H3K4me3^-$ and $H3K27Ac^-$). Read distribution plots (Figure 2B) around MEF2B-bound regions in promoters, intragenic and intergenic regions were created by centering a 6 kb window on the midpoint of peaks and dividing it into 100 bp bins. Histone mark reads found in the 6 kb window were used to produce a binned count distribution. Bin read counts were normalized to reads per million (RPM) and the average RPM per bin was plotted.

In order to identify genes associated with MEF2B-bound regions we considered as candidate genes regulated by MEF2B those that displayed binding in their promoter (topologically defined as −2/+1 kb from the TSS) or were the closest (5’ or 3’) to an intergenic peak (Table S2).

DNA binding motif analysis

DNA binding motif enrichment was calculated comparing a 200 bp window centered on the midpoint of each bound region identified by ChIP-seq analysis, with a background made of randomly sampled genomic sequences that maintain the same size and GC content. Motifs are represented as position-specific weighted scoring matrices (PWM). Each base frequency matrix was converted to probabilities and used to compute a log-likelihood binding score by taking the base 2 logarithm of the sum of the estimated probability for each base divided by the background probability of the base.

Southern Blot analysis

High molecular weight genomic DNA (4 μg) was extracted from frozen tissues by phenol-chloroform extraction and digested with EcoRI overnight at 37°C. The digested DNA was resolved on 0.8% agarose gel followed by transfer to nitrocellulose membrane according to

standard procedures. Hybridization was performed at 37°C o/n using a ^{32}P-labelled JH4 specific probe, as reported (Zhang et al., 2017).

QUANTIFICATION AND STATISTICAL ANALYSIS

Statistics

GraphPad Prism v.6.0 software was used for statistical analyses. One-way analysis of variance (ANOVA) paired with Tukey's multiple-comparison test, Mann-Whitney test or unpaired two-tailed t-test were used to assess statistically significant differences between groups. Fisher's Exact test and Gehan-Breslow-Wilcoxon test were used to assess significance of tumor incidence and mice survival, respectively. Differential expression analyses of RNA-seq data were performed using Student's T-test. Detailed information of the statistical test, number of replicates and number of animals (defined as n) used in each experiment, as well as the definition of center and dispersion are reported in the figure legends. Significance was associated to a $p \leq 0.05$.

Supplementary Material

Refer to Web version on PubMed Central for supplementary material.

ACKNOWLEDGMENTS

We would like to thank Tongwei Mo for mouse husbandry and Michelle Wu and Hongyan Tang for technical support. Dr. Olson kindly provided the *Mef2a*$^{fl/+}$;*Mef2c*$^{fl/+}$;*Mef2d*$^{fl/+}$ compound mice. We are grateful to Carol Ying, David Dominguez-Sola, Wei Gu and Adolfo A. Ferrando for suggestions and discussion. P.B. was partially supported by the European Institute of Oncology (IEO) and the Italian Association for Cancer Research (AIRC). These studies were supported by N.I.H. grants R35CA-210105 (to R.D.-F.) and R01CA172492 (to L.P.) and used the resources of the Herbert Irving Comprehensive Cancer Center (HICCC) Flow Core Facility funded in part through Center Grant P30CA013696; the HICCC Transgenic Mouse Facility; the Columbia University Genome Center; the Taplin Mass Spectrometry Facility, Cell Biology Department, Harvard Medical School.

REFERENCES

(1997). A clinical evaluation of the International Lymphoma Study Group classification of non-Hodgkin's lymphoma. The Non-Hodgkin's Lymphoma Classification Project. Blood 89, 3909–3918. [PubMed: 9166827]

Amendola M, Venneri MA, Biffi A, Vigna E, and Naldini L (2005). Coordinate dual-gene transgenesis by lentiviral vectors carrying synthetic bidirectional promoters. Nat Biotechnol 23, 108–116. [PubMed: 15619618]

Anders S, Pyl PT, and Huber W (2015). HTSeq--a Python framework to work with high-throughput sequencing data. Bioinformatics 31, 166–169. [PubMed: 25260700]

Banumathy G, Somaiah N, Zhang R, Tang Y, Hoffmann J, Andrake M, Ceulemans H, Schultz D, Marmorstein R, and Adams PD (2009). Human UBN1 is an ortholog of yeast Hpc2p and has an essential role in the HIRA/ASF1a chromatin-remodeling pathway in senescent cells. Mol Cell Biol 29, 758–770. [PubMed: 19029251]

Basso K, and Dalla-Favera R (2010). BCL6: master regulator of the germinal center reaction and key oncogene in B cell lymphomagenesis. Adv Immunol 105, 193–210. [PubMed: 20510734]

Basso K, and Dalla-Favera R (2015). Germinal centres and B cell lymphomagenesis. Nat Rev Immunol 15, 172–184. [PubMed: 25712152]

Bea S, Valdes-Mas R, Navarro A, Salaverria I, Martin-Garcia D, Jares P, Gine E, Pinyol M, Royo C, Nadeu F, et al. (2013). Landscape of somatic mutations and clonal evolution in mantle cell lymphoma. Proc Natl Acad Sci U S A 110, 18250–18255. [PubMed: 24145436]

Black BL, and Olson EN (1998). Transcriptional control of muscle development by myocyte enhancer factor-2 (MEF2) proteins. Annu Rev Cell Dev Biol 14, 167–196. [PubMed: 9891782]

Blecher-Gonen R, Barnett-Itzhaki Z, Jaitin D, Amann-Zalcenstein D, Lara-Astiaso D, and Amit I (2013). High-throughput chromatin immunoprecipitation for genome-wide mapping of in vivo protein-DNA interactions and epigenomic states. Nat Protoc 8, 539–554. [PubMed: 23429716]

Bunting KL, Soong TD, Singh R, Jiang Y, Beguelin W, Poloway DW, Swed BL, Hatzi K, Reisacher W, Teater M, et al. (2016). Multi-tiered Reorganization of the Genome during B Cell Affinity Maturation Anchored by a Germinal Center-Specific Locus Control Region. Immunity 45, 497–512. [PubMed: 27637145]

Casola S, Cattoretti G, Uyttersprot N, Koralov SB, Seagal J, Hao Z, Waisman A, Egert A, Ghitza D, and Rajewsky K (2006). Tracking germinal center B cells expressing germ-line immunoglobulin gamma1 transcripts by conditional gene targeting. Proc Natl Acad Sci U S A 103, 7396–7401. [PubMed: 16651521]

Creyghton MP, Cheng AW, Welstead GG, Kooistra T, Carey BW, Steine EJ, Hanna J, Lodato MA, Frampton GM, Sharp PA, et al. (2010). Histone H3K27ac separates active from poised enhancers and predicts developmental state. Proc Natl Acad Sci U S A 107, 21931–21936. [PubMed: 21106759]

Dominguez-Sola D, Kung J, Holmes AB, Wells VA, Mo T, Basso K, and Dalla-Favera R (2015). The FOXO1 Transcription Factor Instructs the Germinal Center Dark Zone Program. Immunity 43, 1064–1074. [PubMed: 26620759]

Epstein AL, Levy R, Kim H, Henle W, Henle G, and Kaplan HS (1978). Biology of the human malignant lymphomas. IV. Functional characterization of ten diffuse histiocytic lymphoma cell lines. Cancer 42, 2379–2391. [PubMed: 214220]

Ernst J, Kheradpour P, Mikkelsen TS, Shoresh N, Ward LD, Epstein CB, Zhang X, Wang L, Issner R, Coyne M, et al. (2011). Mapping and analysis of chromatin state dynamics in nine human cell types. Nature 473, 43–49. [PubMed: 21441907]

Fischle W, Emiliani S, Hendzel MJ, Nagase T, Nomura N, Voelter W, and Verdin E (1999). A new family of human histone deacetylases related to Saccharomyces cerevisiae HDA1p. J Biol Chem 274, 11713–11720. [PubMed: 10206986]

Giannopoulou EG, and Elemento O (2011). An integrated ChIP-seq analysis platform with customizable workflows. BMC Bioinformatics 12, 277. [PubMed: 21736739]

Gossett LA, Kelvin DJ, Sternberg EA, and Olson EN (1989). A new myocyte-specific enhancer-binding factor that recognizes a conserved element associated with multiple muscle-specific genes. Mol Cell Biol 9, 5022–5033. [PubMed: 2601707]

Han A, He J, Wu Y, Liu JO, and Chen L (2005). Mechanism of recruitment of class II histone deacetylases by myocyte enhancer factor-2. J Mol Biol 345, 91–102. [PubMed: 15567413]

Han A, Pan F, Stroud JC, Youn HD, Liu JO, and Chen L (2003). Sequence-specific recruitment of transcriptional co-repressor Cabin1 by myocyte enhancer factor-2. Nature 422, 730–734. [PubMed: 12700764]

Harrow J, Denoeud F, Frankish A, Reymond A, Chen CK, Chrast J, Lagarde J, Gilbert JG, Storey R, Swarbreck D, et al. (2006). GENCODE: producing a reference annotation for ENCODE. Genome Biol 7 Suppl 1, S4 1–9.

Heintzman ND, Stuart RK, Hon G, Fu Y, Ching CW, Hawkins RD, Barrera LO, Van Calcar S, Qu C, Ching KA, et al. (2007). Distinct and predictive chromatin signatures of transcriptional promoters and enhancers in the human genome. Nat Genet 39, 311–318. [PubMed: 17277777]

Huang da W, Sherman BT, and Lempicki RA (2009). Bioinformatics enrichment tools: paths toward the comprehensive functional analysis of large gene lists. Nucleic Acids Res 37, 1–13. [PubMed: 19033363]

Khiem D, Cyster JG, Schwarz JJ, and Black BL (2008). A p38 MAPK-MEF2C pathway regulates B-cell proliferation. Proc Natl Acad Sci U S A 105, 17067–17072 [PubMed: 18955699]

Kraus M, Alimzhanov MB, Rajewsky N, and Rajewsky K (2004). Survival of resting mature B lymphocytes depends on BCR signaling via the Igalpha/beta heterodimer. Cell 117, 787–800. [PubMed: 15186779]

Langmead B, Trapnell C, Pop M, and Salzberg SL (2009). Ultrafast and memory-efficient alignment of short DNA sequences to the human genome. Genome Biol 10, R25. [PubMed: 19261174]

Lefranc MP (2011). IMGT, the International ImMunoGeneTics Information System. Cold Spring Harb Protoc 2011, 595–603. [PubMed: 21632786]

Lei X, Kou Y, Fu Y, Rajashekar N, Shi H, Wu F, Xu J, Luo Y, and Chen L (2018). The Cancer Mutation D83V Induces an alpha-Helix to beta-Strand Conformation Switch in MEF2B. J Mol Biol 430, 1157–1172. [PubMed: 29477338]

Li H, and Durbin R (2009). Fast and accurate short read alignment with Burrows-Wheeler transform. Bioinformatics 25, 1754–1760. [PubMed: 19451168]

Liao Y, Smyth GK, and Shi W (2014). featureCounts: an efficient general purpose program for assigning sequence reads to genomic features. Bioinformatics 30, 923–930. [PubMed: 24227677]

Lohr JG, Stojanov P, Lawrence MS, Auclair D, Chapuy B, Sougnez C, Cruz-Gordillo P, Knoechel B, Asmann YW, Slager SL, et al. (2012). Discovery and prioritization of somatic mutations in diffuse large B-cell lymphoma (DLBCL) by whole-exome sequencing. Proc Natl Acad Sci U S A 109, 3879–3884. [PubMed: 22343534]

Loven J, Hoke HA, Lin CY, Lau A, Orlando DA, Vakoc CR, Bradner JE, Lee TI, and Young RA (2013). Selective inhibition of tumor oncogenes by disruption of super-enhancers. Cell 153, 320–334. [PubMed: 23582323]

Lu J, McKinsey TA, Nicol RL, and Olson EN (2000a). Signal-dependent activation of the MEF2 transcription factor by dissociation from histone deacetylases. Proc Natl Acad Sci U S A 97, 4070–4075. [PubMed: 10737771]

Lu J, McKinsey TA, Zhang CL, and Olson EN (2000b). Regulation of skeletal myogenesis by association of the MEF2 transcription factor with class II histone deacetylases. Mol Cell 6, 233–244. [PubMed: 10983972]

McDonnell TJ, Deane N, Platt FM, Nunez G, Jaeger U, McKearn JP, and Korsmeyer SJ (1989). bcl-2-immunoglobulin transgenic mice demonstrate extended B cell survival and follicular lymphoproliferation. Cell 57, 79–88. [PubMed: 2649247]

McKinsey TA, Zhang CL, and Olson EN (2000). Activation of the myocyte enhancer factor-2 transcription factor by calcium/calmodulin-dependent protein kinase-stimulated binding of 14–3-3 to histone deacetylase 5. Proc Natl Acad Sci U S A 97, 14400–14405. [PubMed: 11114197]

Mikkelsen TS, Ku M, Jaffe DB, Issac B, Lieberman E, Giannoukos G, Alvarez P, Brockman W, Kim TK, Koche RP, et al. (2007). Genome-wide maps of chromatin state in pluripotent and lineage-committed cells. Nature 448, 553–560. [PubMed: 17603471]

Morin RD, Mendez-Lago M, Mungall AJ, Goya R, Mungall KL, Corbett RD, Johnson NA, Severson TM, Chiu R, Field M, et al. (2011). Frequent mutation of histone-modifying genes in non-Hodgkin lymphoma. Nature 476, 298–303. [PubMed: 21796119]

Okosun J, Bodor C, Wang J, Araf S, Yang CY, Pan C, Boller S, Cittaro D, Bozek M, Iqbal S, et al. (2014). Integrated genomic analysis identifies recurrent mutations and evolution patterns driving the initiation and progression of follicular lymphoma. Nat Genet 46, 176–181. [PubMed: 24362818]

Pan F, Means AR, and Liu JO (2005). Calmodulin-dependent protein kinase IV regulates nuclear export of Cabin1 during T-cell activation. EMBO J 24, 2104–2113. [PubMed: 15902271]

Pasqualucci L, Khiabanian H, Fangazio M, Vasishtha M, Messina M, Holmes AB, Ouillette P, Trifonov V, Rossi D, Tabbo F, et al. (2014). Genetics of follicular lymphoma transformation. Cell reports 6, 130–140. [PubMed: 24388756]

Pasqualucci L, Trifonov V, Fabbri G, Ma J, Rossi D, Chiarenza A, Wells VA, Grunn A, Messina M, Elliot O, et al. (2011). Analysis of the coding genome of diffuse large B-cell lymphoma. Nat Genet 43, 830–837. [PubMed: 21804550]

Pertea M, Kim D, Pertea GM, Leek JT, and Salzberg SL (2016). Transcript-level expression analysis of RNA-seq experiments with HISAT, StringTie and Ballgown. Nat Protoc 11, 1650–1667. [PubMed: 27560171]

Pon JR, and Marra MA (2016). MEF2 transcription factors: developmental regulators and emerging cancer genes. Oncotarget 7, 2297–2312. [PubMed: 26506234]

Pon JR, Wong J, Saberi S, Alder O, Moksa M, Grace Cheng SW, Morin GB, Hoodless PA, Hirst M, and Marra MA (2015). MEF2B mutations in non-Hodgkin lymphoma dysregulate cell migration by decreasing MEF2B target gene activation. Nat Commun 6, 7953. [PubMed: 26245647]

Potthoff MJ, and Olson EN (2007). MEF2: a central regulator of diverse developmental programs. Development 134, 4131–4140. [PubMed: 17959722]

Reddy A, Zhang J, Davis NS, Moffitt AB, Love CL, Waldrop A, Leppa S, Pasanen A, Meriranta L, Karjalainen-Lindsberg ML, et al. (2017). Genetic and Functional Drivers of Diffuse Large B Cell Lymphoma. Cell 171, 481–494 e415. [PubMed: 28985567]

Ryan RJ, Drier Y, Whitton H, Cotton MJ, Kaur J, Issner R, Gillespie S, Epstein CB, Nardi V, Sohani AR, et al. (2015). Detection of Enhancer-Associated Rearrangements Reveals Mechanisms of Oncogene Dysregulation in B-cell Lymphoma. Cancer Discov 5, 1058–1071. [PubMed: 26229090]

Schindelin J, Rueden CT, Hiner MC, and Eliceiri KW (2015). The ImageJ ecosystem: An open platform for biomedical image analysis. Mol Reprod Dev 82, 518–529. [PubMed: 26153368]

Schwickert TA, Alabyev B, Manser T, and Nussenzweig MC (2009). Germinal center reutilization by newly activated B cells. J Exp Med 206, 2907–2914. [PubMed: 19934021]

Shaffer AL, 3rd, Young RM, and Staudt LM (2012). Pathogenesis of human B cell lymphomas. Annu Rev Immunol 30, 565–610. [PubMed: 22224767]

Subramanian A, Tamayo P, Mootha VK, Mukherjee S, Ebert BL, Gillette MA, Paulovich A, Pomeroy SL, Golub TR, Lander ES, and Mesirov JP (2005). Gene set enrichment analysis: a knowledge-based approach for interpreting genome-wide expression profiles. Proc Natl Acad Sci U S A 102, 15545–15550. [PubMed: 16199517]

Swerdlow SH, Campo E, Harris NL, Jaffe ES, Pileri SA, Stein H, Thiele J (2016). WHO Classification of Tumors of Haematopoietic and Lymphoid Tissues, (Lyon: International Agency for Research on Cancer (IARC) Publications).

Tagami H, Ray-Gallet D, Almouzni G, and Nakatani Y (2004). Histone H3.1 and H3.3 complexes mediate nucleosome assembly pathways dependent or independent of DNA synthesis. Cell 116, 51–61. [PubMed: 14718166]

Victora GD, Dominguez-Sola D, Holmes AB, Deroubaix S, Dalla-Favera R, and Nussenzweig MC (2012). Identification of human germinal center light and dark zone cells and their relationship to human B-cell lymphomas. Blood 120, 2240–2248. [PubMed: 22740445]

Victora GD, Schwickert TA, Fooksman DR, Kamphorst AO, Meyer-Hermann M, Dustin ML, and Nussenzweig MC (2010). Germinal center dynamics revealed by multiphoton microscopy with a photoactivatable fluorescent reporter. Cell 143, 592–605. [PubMed: 21074050]

Whyte WA, Orlando DA, Hnisz D, Abraham BJ, Lin CY, Kagey MH, Rahl PB, Lee TI, and Young RA (2013). Master transcription factors and mediator establish super-enhancers at key cell identity genes. Cell 153, 307–319. [PubMed: 23582322]

Wilker PR, Kohyama M, Sandau MM, Albring JC, Nakagawa O, Schwarz JJ, and Murphy KM (2008). Transcription factor Mef2c is required for B cell proliferation and survival after antigen receptor stimulation. Nat Immunol 9, 603–612. [PubMed: 18438409]

Ying CY, Dominguez-Sola D, Fabi M, Lorenz IC, Hussein S, Bansal M, Califano A, Pasqualucci L, Basso K, and Dalla-Favera R (2013). MEF2B mutations lead to deregulated expression of the oncogene BCL6 in diffuse large B cell lymphoma. Nat Immunol 14, 1084–1092. [PubMed: 23974956]

Youn HD, and Liu JO (2000). Cabin1 represses MEF2-dependent Nur77 expression and T cell apoptosis by controlling association of histone deacetylases and acetylases with MEF2. Immunity 13, 85–94. [PubMed: 10933397]

Zhang J, Grubor V, Love CL, Banerjee A, Richards KL, Mieczkowski PA, Dunphy C, Choi W, Au WY, Srivastava G, et al. (2013). Genetic heterogeneity of diffuse large B-cell lymphoma. Proc Natl Acad Sci U S A 110, 1398–1403. [PubMed: 23292937]

Zhang J, Vlasevska S, Wells VA, Nataraj S, Holmes AB, Duval R, Meyer SN, Mo T, Basso K, Brindle PK, et al. (2017). The CREBBP Acetyltransferase Is a Haploinsufficient Tumor Suppressor in B-cell Lymphoma. Cancer Discov 7, 322–337. [PubMed: 28069569]

HIGHLIGHTS

- MEF2B promotes the formation of Germinal Centers (GC)
- MEF2B modulates GC-master regulator genes and GC-specific enhancers
- The lymphoma-associated MEF2B^{D83V} mutant escapes binding by co-repressors
- Expression of MEF2B^{D83V} causes GC expansion and contributes to lymphomagenesis

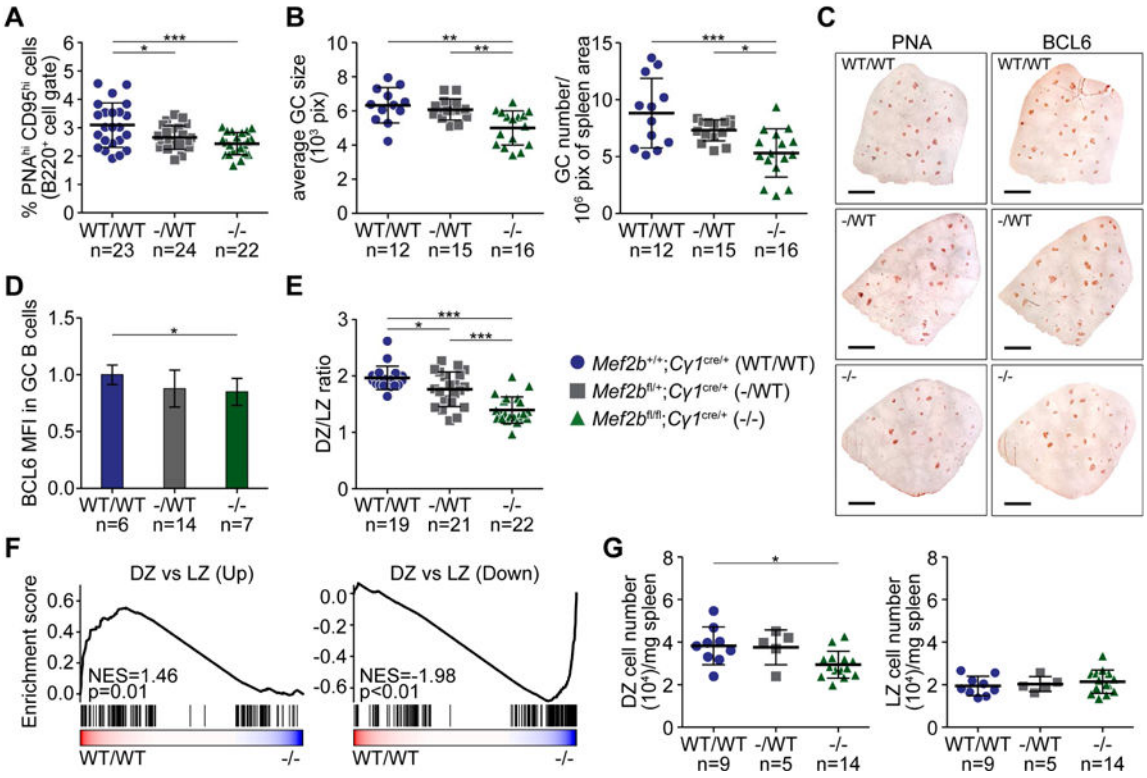

Figure 1. GC-specific deletion of *Mef2b* reduces GC formation and DZ/LZ ratio.

(A) Percentage of splenic GC B cells in *Mef2b*$^{+/+}$;*Cγ1*$^{cre/+}$ (WT/WT), *Mef2b*$^{fl/+}$;*Cγ1*$^{cre/+}$ (-/WT) and *Mef2b*$^{fl/fl}$;*Cγ1*$^{cre/+}$ (−/−) littermates, as measured by flow cytometry 10 days post-SRBC immunization. **(B)** Average GC size and numbers measured by pixels (pix) quantitation of immunofluorescence staining for the GC marker PNA on FFPE spleen sections. Analysis was performed on a subset of the mice displayed in panel A. **(C)** Immunohistochemistry for PNA and BCL6 on representative spleen sections. Scale bar, 2000 μm. **(D)** BCL6 mean fluorescence intensity (MFI) in GC B cells (B220^{+}/PNA^{hi}/CD95^{hi}) measured by flow cytometry analysis and displayed as fold change relative to WT mice (Mann-Whitney test, *p≤0.05). **(E)** DZ (CXCR4^{hi}/CD86^{lo})/LZ (CXCR4^{lo}/CD86^{hi}) ratios in GC B cells (B220^{+}/PNA^{hi}/CD95^{hi}). **(F)** Gene Set Enrichment Analysis (GSEA) in *Mef2b*$^{+/+}$;*Cγ1*$^{cre/+}$ (WT/WT) and *Mef2b*$^{fl/fl}$;*Cγ1*$^{cre/+}$ (−/−) GC B cell RNA-seq data using a previously reported mouse DZ vs LZ gene signature (Victora et al., 2012). NES, Normalized Enrichment Score. **(G)** DZ and LZ B cell numbers normalized by spleen weight in a subset of the mice displayed in panel E.

Dot plots and bar graph display average ± SD. P values in dot plots were determined by one-way ANOVA with Tukey's multiple comparison test (***p≤0.001, **p≤0.01, *p≤0.05).

See also Figures S1 and S2 and Table S1.

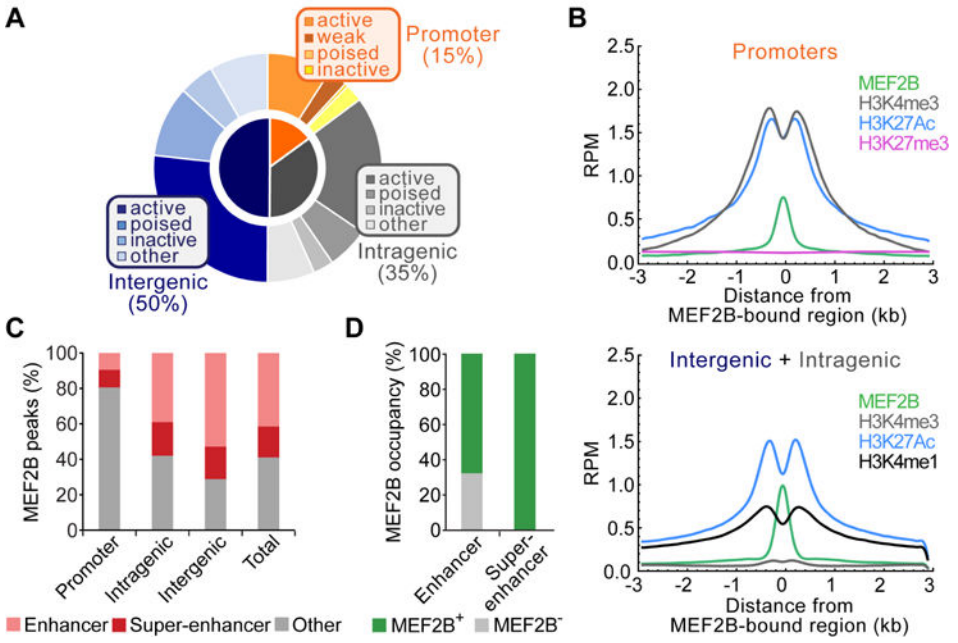

Figure 2. MEF2B genome-wide DNA binding in human GC B cells.

(A) MEF2B peak distribution relative to the closest transcription start site (TSS). Promoters are defined as the regions encompassing the TSS (−2/+1 kb) and classified based on their chromatin marks as active (H3K4me3^{+}, H3K27me3^{-} and H3K27Ac^{+}), weak (H3K4me3^{+}, H3K27me3^{-} and H3K27Ac^{-}), poised (H3K4me3^{+} and H3K27me3^{+}), or inactive (H3K4me3^{-}). Intragenic and intergenic regions are classified based on enhancer-associated chromatin marks as active (H3K4me1^{+}, H3K4me3^{-}, and H3K27Ac^{+}) or poised (H3K4me1^{+}, H3K4me3^{-} and H3K27Ac^{-}), while considered inactive when lacking all marks (H3K4me1^{-}, H3K4me3^{-} and H3K27Ac^{-}). The term “other” refers to regions that do not fulfill the above classification criteria. **(B)** Distribution of reads (as reads per million, RPM) for the indicated histone marks, relative to the MEF2B peaks. The displayed histone modifications are the same used in panel A to classify bound regions in promoters (H3K4me3, H3K27me3 and H3K27Ac) or intra/intergenic regions (H3K4me1, H3K4me3 and H3K27Ac). **(C)** Percentage of MEF2B peaks that are located in enhancers and super-enhancers, as identified by the ROSE algorithm applied to H3K27Ac data obtained from normal GC B cells. “Other” denotes all remaining regions. **(D)** Percentage of GC enhancers and super-enhancers that are occupied by MEF2B.

See also Tables S2 and S3.

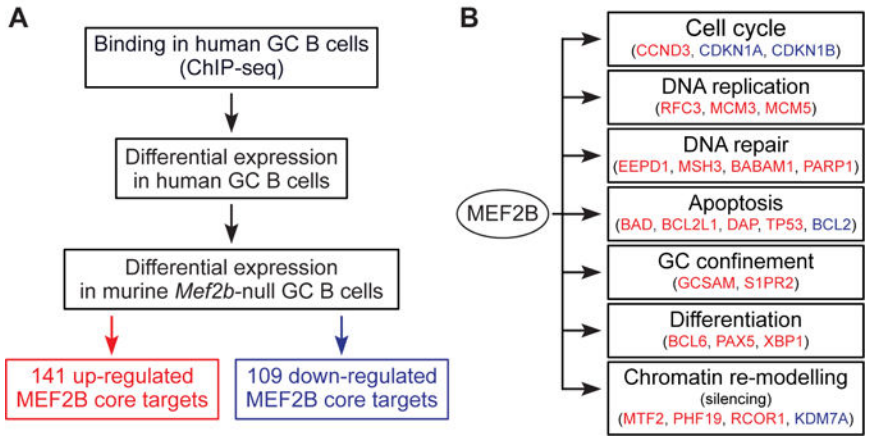

Figure 3. MEF2B-driven transcriptional network in GC B cells.

(A) Flowchart detailing the main steps leading to the identification of MEF2B targets as bound in regulatory regions, transcriptionally regulated during the human GC transition, and affected by *Mef2b* deletion in mouse GC B cells. **(B)** Schematic representation of the main pathways affected by MEF2B as obtained by integrating manual annotations of the genes identified in panel A and the results of pathway enrichment analysis performed using the DAVID 6.7 tool and KEGG, Biocarta, Panther and Reactome databases. The genes included among the 141 up-regulated or 109 down-regulated core targets are displayed in red and blue, respectively.

See also Tables S4.

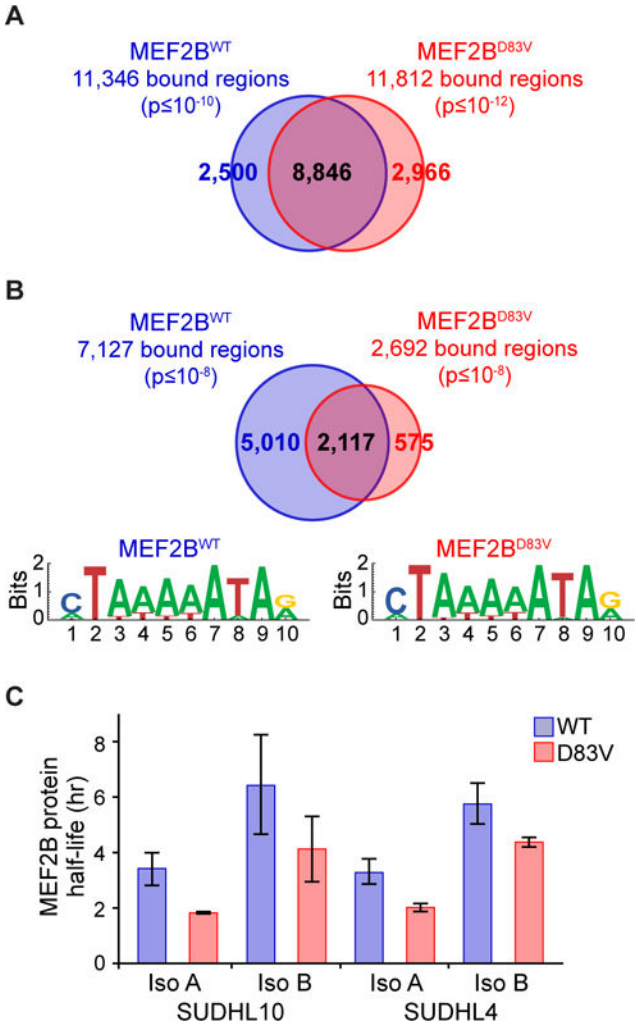

Figure 4. MEF2B^{D83V} displays hypomorphic features including reduced DNA binding and protein stability.

(A-B) Venn diagram illustrating the overlap between DNA regions bound by MEF2B^{WT} or MEF2B^{D83V} mutant, as identified by ChIP-sequencing analysis with anti-MEF2B or anti-FLAG and –HA **(B)** antibodies in SUDHL10-FLAG-HA-MEF2B^{WT} or -MEF2B^{D83V} cell lines. Motif logos summarize the MEF2 DNA motifs found in the regions bound by MEF2B^{WT} or MEF2B^{D83V}. **(C)** MEF2B^{WT} and MEF2B^{D83V} protein half-life as measured in SUDHL10 or SUDHL4 cell lines expressing FLAG-HA-MEF2B^{WT} or -MEF2B^{D83V} isoform A or isoform B upon treatment with cycloheximide. Data are displayed as average ± SD of at least two independent experiments.

See also Figure S3 and Table S5.

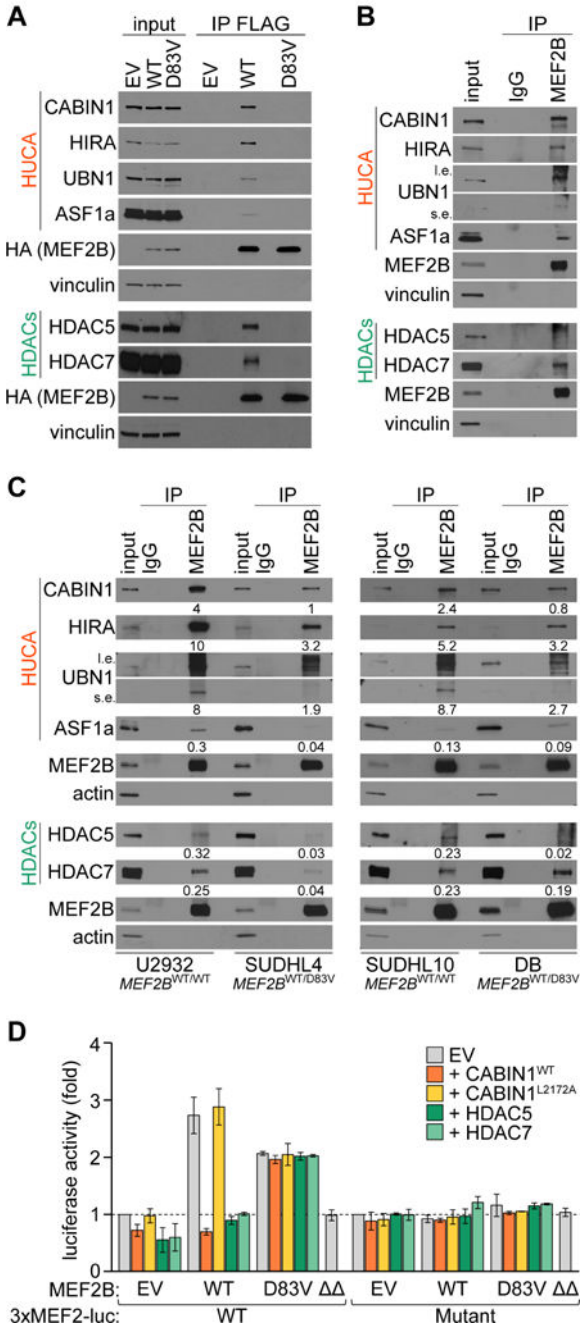

Figure 5. MEF2B^{D83V} mutant escapes binding to and repression by the HUCA complex and HDACs class IIa.

(A) Immunoblot analysis of MEF2B interactors upon co- immunoprecipitation (IP) with anti-FLAG antibody in SUDHL10-FLAG-HA-MEF2B^{WT} or - MEF2B^{D83V} cells. Input is 10% of total lysate used for IP. EV, Empty Vector. **(B-C)** Immunoblot analyses of normal human GC B cells **(B)** and U2932 (*MEF2B*$^{WT/WT}$), SUDHL4 (*MEF2B*$^{WT/D83V}$), SUDHL10 (*MEF2B*$^{WT/WT}$), DB (*MEF2B*$^{WT/D83V}$) DLBCL cell lines **(C)** before (input; 10% of total sample) and after IP with anti-MEF2B antibody or IgG. Numbers under immunoblots represent IP enrichment relative to the input, as measured by densitometry. **(D)** Luciferase

activity driven by synthetic wild-type (WT) or mutated (Mutant) MEF2 binding sites (3xMEF2-luc), as measured in HEK293T cells upon transfection with EV or plasmids expressing $MEF2B^{WT}$, $MEF2B^{D83V}$ or $MEF2B^{\Delta MADSMEF}$ (ΔΔ) mutants alone or with $CABIN1^{WT}$, $CABIN1^{L2172A}$, HDAC5 or HDAC7. Data are shown as average ± SD of two independent experiments relative to EV control. Significant differences were assessed by unpaired two- tailed t-test ($MEF2B^{WT}$- or $MEF2B^{D83V}$-driven inductions vs EV control $p \leq 0.001$; CABIN1, HDAC5 or HDAC7-mediated repressions of $MEF2B^{WT}$-driven induction $p \leq 0.01$).
See also Figure S4.

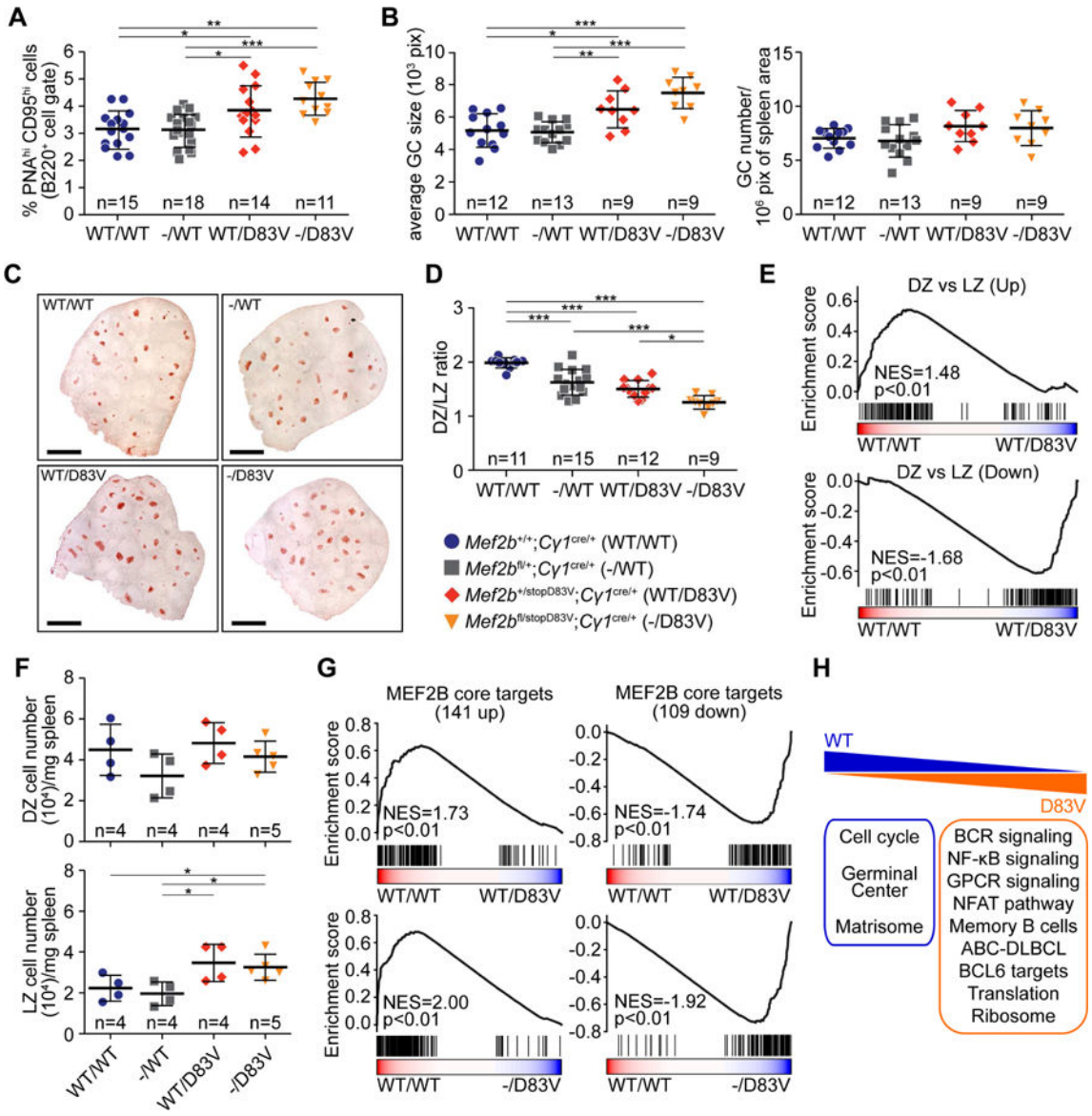

Figure 6. The *Mef2b*^{D83V} mutant allele acts dominantly in GC formation.

(A) Percentage of splenic GC B cells (PNA^{hi}/CD95^{hi}) in *Mef2b*$^{+/+}$;*Cγ1*$^{cre/+}$ (WT/WT), *Mef2b*$^{fl/+}$;*Cγ1*$^{cre/+}$ (-/WT), *Mef2b*$^{+/stopD83V}$;*Cγ1*$^{cre/+}$ (WT/D83V) and *Mef2b*$^{fl/stopD83V}$;*Cγ1*$^{cre/+}$ (-/D83V) mice, as measured by flow cytometry 10 days post-SRBC immunization. **(B)** Average GC size and numbers as measured by pixels (pix) quantitation of immunofluorescence staining for the GC marker PNA on FFPE spleen sections in a subset of the mice displayed in panel A. **(C)** Immunohistochemistry for PNA on representative spleen sections. Scale bar, 2000 μm. **(D)** DZ (CXCR4^{hi}/CD86^{lo})/LZ (CXCR4^{lo}/CD86^{hi}) ratios in GC B cells (B220^{+}/PNA^{hi}/CD95^{hi}). **(E)** Gene Set Enrichment Analysis (GSEA) in *Mef2b*$^{+/+}$;*Cγ1*$^{cre/+}$ (WT/WT) and *Mef2b*$^{+/stopD83V}$;*Cγ1*$^{cre/+}$ (WT/D83V) GC B cell RNA-seq data using a previously reported mouse DZ vs LZ gene signature (Victora et al., 2012). NES, Normalized Enrichment Score. **(F)** DZ and LZ B cell numbers normalized by spleen weight in a subset of the mice displayed in panel D (Mann-Whitney

test, *p≤0.05). **(G)** GSEA of the MEF2B core targets (as identified in Figure 3A) in the GC B cell transcriptional profiles of *Mef2b*$^{+/+}$;*Cγ1*$^{cre/+}$ (WT/WT), *Mef2b*$^{+/stopD83V}$;*Cγ1*$^{cre/+}$ (WT/D83V) and *Mef2b*$^{fl/stopD83V}$;*Cγ1*$^{cre/+}$ (-/D83V) mice. **(H)** Schematic representation of the results of the pathway enrichment analysis performed on RNA-seq profiles of GC B cells from *Mef2b*$^{+/+}$;*Cγ1*$^{cre/+}$ (WT/WT) compared to *Mef2b*$^{+/stopD83V}$;*Cγ1*$^{cre/+}$ (WT/D83V) and *Mef2b*$^{fl/stopD83V}$;*Cγ1*$^{cre/+}$ (-/D83V) 4 mice each, using GSEA and MSigDB and SignatureDB databases.Dot plots display average ± SD. P values in dot plots were determined by one-way ANOVA with Tukey's multiple comparison test (***p≤0.001, **p≤0.01, *p≤0.05), unless otherwise specified.

See also Figure S5 and Tables S6-S8.

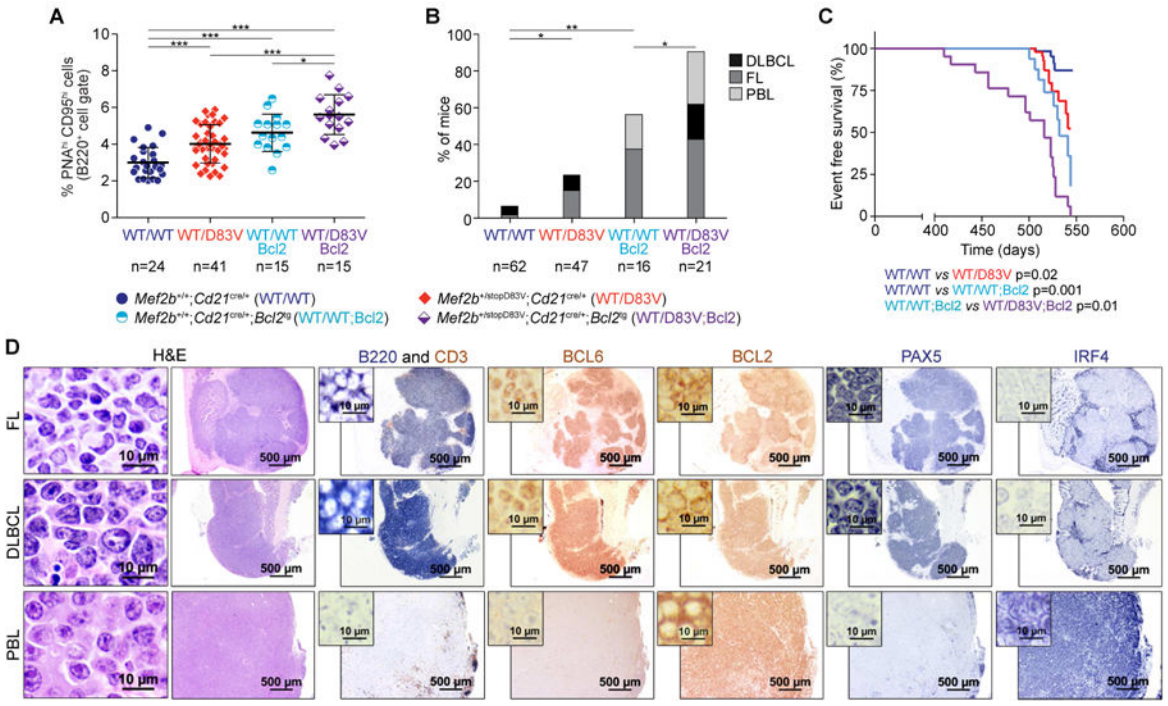

Figure 7. MEF2B^{D83V} expression in mice leads to the development of B cell lymphomas.

(A) Percentage of splenic GC B cells (PNA^{hi}/CD95^{hi}) in *Mef2b*$^{+/+}$;*CD21*$^{cre/+}$ (WT/WT), *Mef2b*$^{+/stopD83V}$;*CD21*$^{cre/+}$ (WT/D83V),*Mef2b*$^{+/+}$;*CD21*$^{cre/+}$;*Bcl2*^{tg} (WT/WT;Bcl2), *Mef2b*$^{+/stopD83V}$;*CD21*$^{cre/+}$;*Bcl2*^{tg} (WT/D83V; Bcl2) mice, as measured by flow cytometric analysis in 3-month-old mice 10 days after a single SRBC immunization. Data are displayed as dot plots, including average ± SD. $^{***}p\leq0.001$, $^{*}p\leq0.05$ (one-way ANOVA with Tukey's multiple comparison test). **(B)** Frequency of development of B cell lymphomas in the animals with the indicated genotypes. Colored bars indicate different diagnosis, namely Follicular Lymphomas (FL), Diffuse Large B Cell Lymphomas (DLBCL) and Plasmablastic lymphoma (PBL). $^{**}p\leq0.01$, $^{*}p\leq0.05$ (Fisher's Exact test). **(C)** Event-free survival curve of mice reported in panel (B) (Gehan-Breslow-Wilcoxon test). **(D)** Hematoxylin and eosin (H&E) staining and immunohistochemical analysis of representative tumors from mice diagnosed with FL, DLBCL or PBL.See also Figure S6.